Chapter 3

Molybdenum: A Rear Gateway of CIGS Solar Cell Module

3.0 Motivation, Objective, and Abstract

Motivation

Back ohmic contact is the rear gateway of selective charge carriers. For CIGS solar cell module, the Molybdenum (Mo) layer act dominantly among other ohmic back contact materials in terms of performance enhancer and reliability. Therefore, Mo layer has been scrutinized comprehensively as an ohmic back contact with the available research laboratory's deposition facility.

Objective

- To deposit Mo ohmic back contact by DC sputtering on processed cleaned 60 x 60 x 1 mm SLG substrate under different deposition conditions.
- To evaluate Mo layer physical, microstructure, and optoelectronic properties and adhesion test (by LASER) suitable for CIGS solar cell module.
- To optimize the Mo layer to withstand the chemical deposition process.
- To probe Laser interaction with deposited Mo layer and enumerate several Lasers parameters to achieve clean P1 scribe isolation.

Abstract

Single and bilayer Molybdenum (Mo) thin films as an ohmic back-contact for CIGS solar cell modules have been investigated. Using DC sputtering technique, single layer Mo thin films at 10 mTorr and 1 mTorr while bilayer Mo thin films having a bottom layer with pressure 10 mTorr and the top layer with pressure 1 mTorr have been deposit. DC power was upheld to (50, 100, 150, 200 W) approximately. Ohmic back-contact Mo layers were examined for their structural, optical, electrical, microstructural, and mechanical properties. Deliberate heating was provided to bilayer Mo thin films to deposit at substrate temperature 215 °C. Characterization results reveal that bilayer Mo thin film deposited at power 150 W has a dense structure, compressive stress, high

reflection (72 %), and sheet resistance (0.332 Ω/□). Adhesion test was performed on single and bilayer Mo thin films. It was observed that the Mo bilayer thin film deposited at 150 W adheres more to a glass substrate compared to Mo thin film at other power. In conclusion, it has been noticed that bilayer Mo thin films deposited at 150 W and substrate temperature as room temperature as well as 215 °C with the thickness of 0.5 µm each (top and bottom) layer has significant dense columnar growth, which is desirable for the back-contact of CIGS solar cell module. There is no significant (growth is similar) change in bilayer Mo thin film properties deposited at room temperature (RT) and substrate temperature 215 °C. For the monolithic interconnection of the CIGS solar cell module, the first step is P1 scribing on the Mo layer. Using Nd:YAG 1064 nm nanosecond laser and two different optical setups, first using YAG focusing lens and second YAG f-theta lens with Galvo mirrors, P1 scribing process was investigated and optimized. Several parameters such as laser power, pulse repetition rate, scan speed, pass delay, and depth of focus were varied to optimize the P1 scribing process.

3.1 An Essential Ohmic Back-Contact: Molybdenum layer

Many researchers used molybdenum as an ohmic back contact for developing heterojunction CIGS solar cell modules. Apart from Mo, Au, Pt, Ni, Ag, and Cu can be used as ohmic back-contact for solar cells [1]. Molybdenum possesses all necessary features to act as a good ohmic back contact like good adhesion, low resistivity, and compatible thermal coefficient of expansion with soda-lime glass (SLG) substrate. Bulk molybdenum has a resistivity of 5.3-5.5 µΩ-cm, Young's modulus 3.43 x 10^{12} dyne/cm^2, yield strength 2.10 x 10^{10} dyne/cm^2, thermal coefficient of expansion 4.8 x 10^6 k^{-1}, and thermal conductivity 1.38 Wcm^{-1}k^{-1} [2]. Industries look forward for dense microstructure, low resistive, and highly adhered Mo back-contact for CIGS solar cell. To date, it is difficult to achieve a single Mo thin film layer that can serve as a good ohmic back-contact. The results for single layer Mo thin films are questionable to produce as a back-ohmic contact. Many physical vapor deposition (PVD) techniques such as E-beam, S-gun, arc-ion plating, RF sputtering, and DC sputtering have been used to deposit Mo thin film [3-6]. Researchers have studied a single Mo layer deposited by DC sputtering technique with a wide range of deposition parameters like pressure, thickness, and different working-gas (Ne, Kr, Ar, Xe) [7, 8]. They found that depositing a single Mo thin film using cylindrical magnetron at high deposition pressure possess tensile stress. An increase in working gas pressure affects the deposition power by voltage drop at fixed current; this reduces the microstructural quality of the Mo thin films. At low deposition pressure, Mo thin films have a low resistance with poor adhesion quality while at high deposition pressure inverse results were observed. This was a limitation for Mo thin film which serves as an ohmic back-contact for solar cells. To overcome such constraints, J. Scofield [9] proposed a bilayer Mo thin film structure, which constitutes the bottom layer (high pressure) and the top layer (low pressure). These bilayer structures comprise all features required for solar cells better performance. The bottom layer gives better adhesion while the top layer provides low resistance. Bilayer Mo thin films have a dense microstructure through which sodium (Na) can have a pathway towards an absorber layer (CIGS) which helps to improve the efficiency of CIGS solar cells [10]. Radio Frequency (RF) sputtering technique has been sampled for depositing Mo thin films. But compared to RF sputtering, the growth structure properties were more enhanced in DC sputtering technique [11].

3.2 Experimental Details

Bilayer Mo thin films have been deposited using the PVD technique in vacuum deposition unit (Hind High Vacuum Pvt. Ltd., India, Model-15F6) system. DC power supply (Hutteinger Electronik Truplasma, Germany, Model-DC3005) with a 2-inch magnetron and Mo target (2inch diameter, 5mm thick) is used to deposit Bilayer Mo thin films on 2 inch-sq soda-lime glass substrate. At constant speed, the substrate was rotated to deposit uniform thickness Mo thin films. The distance between the Mo target and soda-lime glass was 10 cm. Base pressure 10^{-5} mTorr was maintained and argon gas flow was kept constant at 6 sccm and the gas flow was controlled by (MFC) Mass Flow Controller (Aalborg, Germany, Model-GFC 17S-VADL2-A0A). The bottom layer of Mo has been deposited at working pressure 10 mTorr by varying DC power (50, 100, 150, 200 W). Pre-sputtering of Mo target has been carried out for 5 minutes to eliminate surface oxidation. By varying working pressure, the bilayer of the Mo layer at 10 mTorr (bottom layer) and 1 mTorr (top layer) is deposited. The bilayer Mo microstructure with the bottom and the top layer is deposited at DC power (50, 100, 150, 200 W) at room temperature (RT) and substrate temperature (ST) 215 °C. The thickness of each layer is 500 nm. The total thickness of all bilayer Mo microstructure was kept constant at one µm. Thickness was controlled by an in-situ quartz crystal thickness monitor (Sigma Instrument SQC-122). Structural, optical, electrical, microstructural, and mechanical characterizations have been carried out.

3.3 Influence of Sputtering Power

3.3.1 X-Ray Diffraction Analysis

Crystal structure and phase conformation of Mo thin films were analyzed using the X-Ray Diffraction technique. Single Mo thin films deposited at 10 mTorr and 1 mTorr deposition pressure with thickness 500 nm and bilayer Mo thin films deposited at 10 mTorr (bottom) and 1 mTorr (top) deposition pressure with thickness 1 µm at deposition power (50, 100, 150, 200 W) has significantly influenced the phase structure of Mo thin films. No intentional heating was provided to the substrate i. e. substrate was at room temperature. Phase structures of single and bilayer Mo thin films are shown in Fig 3.1(a, b, and c) which shows the presence of the major peak of (*110*) phase of the 2θ values 40 ° with high intensity and sharp peak. XRD analysis depicts that Mo thin films possess cubic structure at (*hkl*) values (110). The phase confirmation has been confirmed with JCPDS card no. (01-1208) [12]. Full- width half-maximum (FWHM) broadening and the difference in intensity peak was observed in Mo thin films deposited at DC power. In Fig 3.1(a) at 2θ values, 39.5 ° another (*hkl*) values (110), and 73 ° (220) phase structure have been observed. At high deposition pressure i. e. 10 mTorr as deposition power increases, major peak intensity increased. Similar phase structures have been observed in Fig 3.1(b) and Fig 3.1(c). There is a difference in sharpness and FWHM broadening of the XRD peaks of single and bilayer Mo thin films deposited at various deposition powers. At 10 mTorr pressure, Mo adatoms possess less kinetic energy due to a small mean free path and more collisions between sputtered Mo atoms and Ar atoms. At higher sputtering power Ar ions bombard against Mo target with high energy, these collisions excite Mo particles from the target with gained kinetic energy. High energy density and energy of charge carriers resulting in a high growth rate with an increase in DC power. All adatoms reaching the substrate surface have high surface energy, which forms a porous structure. Lowering deposition pressure i. e. 1 mTorr, single Mo thin films deposited at deposition power (50, 100, 150, 200 W) thickness of 500 nm at RT possess improved crystallinity. In Fig 3.1(b) other than the major phase i. e. (*110*), at 2θ values, 40.1 ° and secondary phase (*211*) at 70.2 ° peak were observed which is sharp and intense. Improved crystallinity at lower deposition pressure 1 mTorr was manifest by the presence of the secondary phase (*211*). Mo adatoms have a longer pathway to travel between target surface and substrate; a collision between Ar ions and Mo atoms is decreased drastically compared to higher deposition pressure. Sputtering yield increase due to high energy ejection of Mo atoms which in turn increase in growth rate in lower deposition pressure regime. The formation of nucleation sites improves as deposition power increases. Close dense pack structure with less grain boundary has been grown and minimization of the surface energy of Mo adatoms at the substrate surface leads to form coalescence; finally results in the formation of the homogeneous dense structured film. DC power influences the crystallinity of the Mo thin films. More sputtered Mo atoms have ejected from the target surface and travel with highly accelerated kinetic energy gained by the Mo atoms. Bilayer Mo thin films deposited at 10 mTorr (bottom) and 1 mTorr (top) pressure and deposition power (50, 100, 150, 200 W) thickness of 1 µm. Fig 3.1(c) shows the XRD analysis of bilayer Mo thin films. All bilayer Mo thin films possess both major primary (110) and secondary (211) cubic phases. XRD analysis reflects the combined trend of peaks of single Mo thin films deposited at pressure 10 and 1 mTorr. The secondary phase (211) cubic in the bilayer Mo structure has been suppressed compare to the single Mo thin-film phase. In bilayer Mo thin films, the second phase was dominated by high deposition pressure conditions. The FWHM values of bilayer Mo thin films of major peak get smaller compared to a single layer. Phase shift in Mo thin films was observed which is due to voids, structure defects, and strain in bottom Mo thin films. Lattice constant ‘a’ was determined for Mo thin films from the d-spacing value.

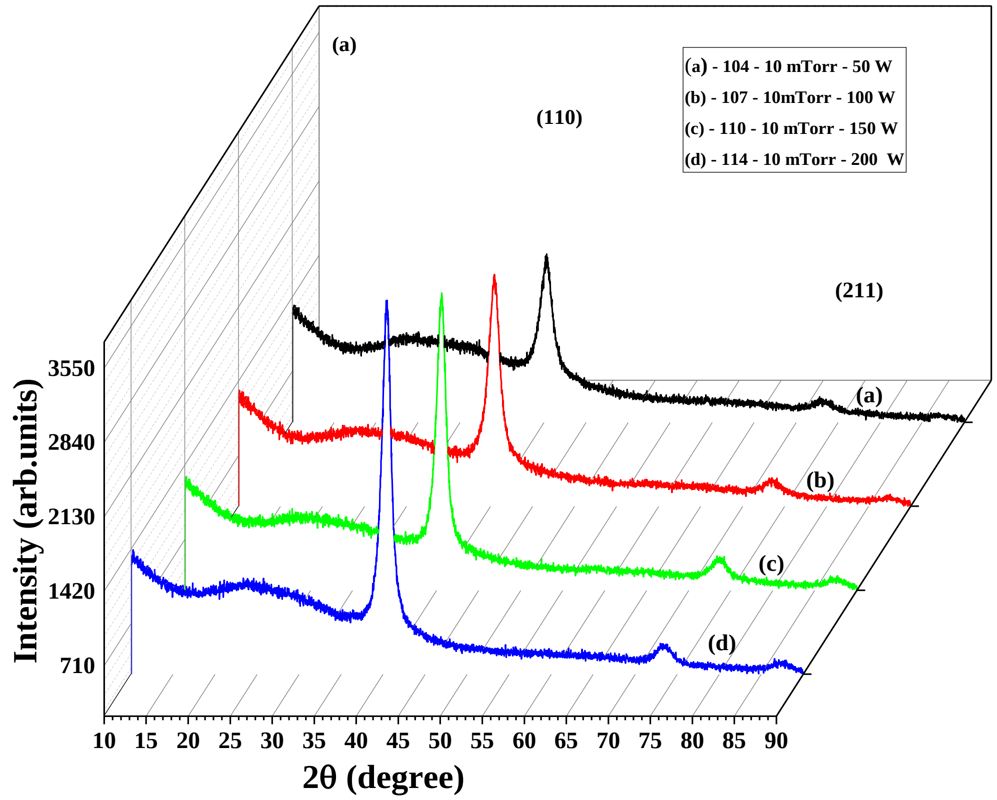
(a)
(a) - 104 - 10 mTorr - 50 W
(b) - 107 - 10mTorr - 100 W
(c) - 110 - 10 mTorr - 150 W
(d) - 114 - 10 mTorr - 200 W
(110)
(211)
(a)
(b)
(c)
(d)
Intensity (arb.units)
3550
2840
2130
1420
710
10 15 20 25 30 35 40 45 50 55 60 65 70 75 80 85 90
2θ (degree)

(a)

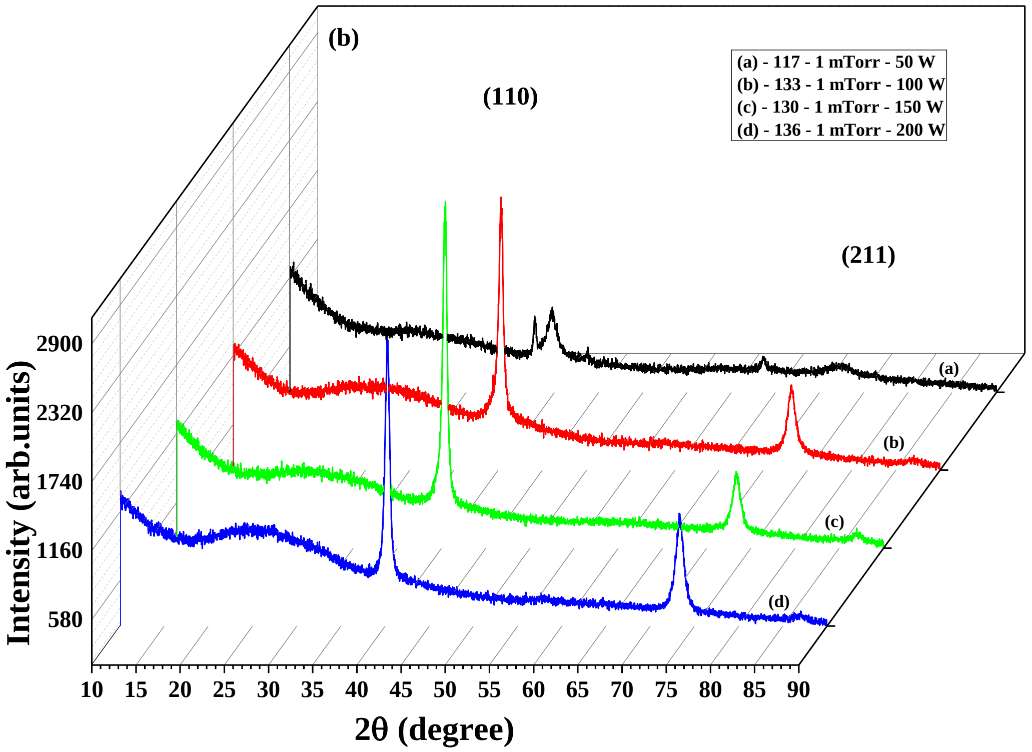
(b)
(a) - 117 - 1 mTorr - 50 W
(b) - 133 - 1 mTorr - 100 W
(c) - 130 - 1 mTorr - 150 W
(d) - 136 - 1 mTorr - 200 W
(110)
(211)
(a)
(b)
(c)
(d)
Intensity (arb.units)
2900
2320
1740
1160
580
10 15 20 25 30 35 40 45 50 55 60 65 70 75 80 85 90
2θ (degree)

(b)

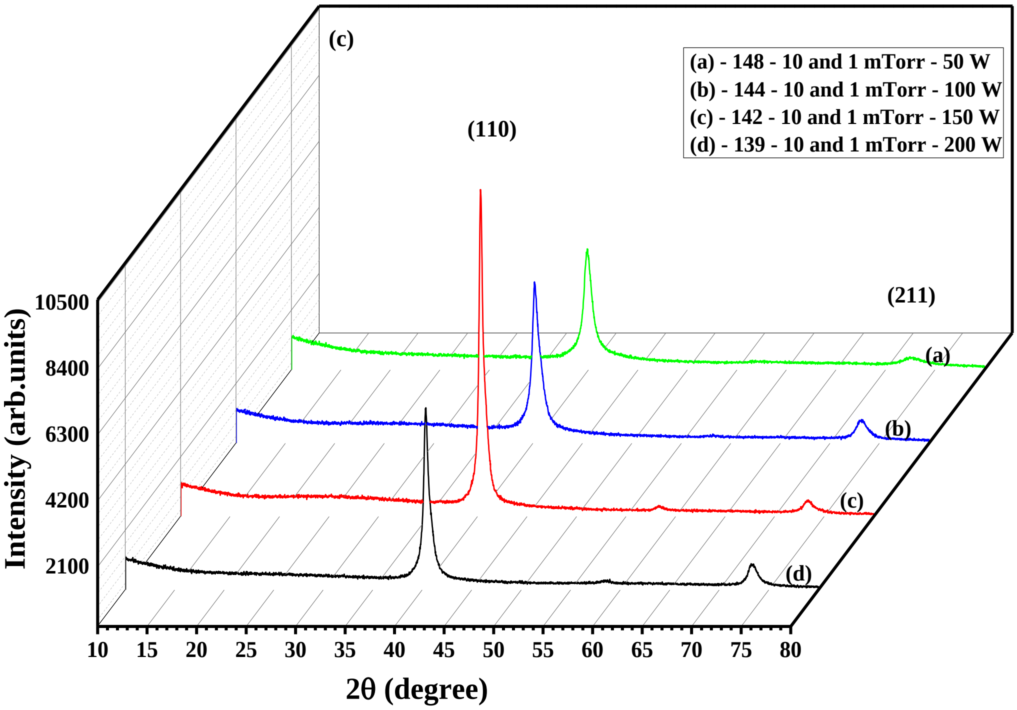

(c)

Fig 3.1: XRD analysis of Mo thin films deposited at (a) 10 mTorr (bottom), (b) 1 mTorr (Top) and (c) 10 mTorr (bottom) and 1 mTorr (Top) at RT with different DC power.

On comparing XRD analysis from Fig 3.1 (a, b, and c), one can say that the crystallinity of Mo thin films is enhanced by depositing two-layer of Mo at different pressure. The d-spacing value for (*hkl*) orientation direction for the cubic structure of Mo thin films with lattice constant was determined by the following equation (3.1) mentioned below:

$$d = \frac{a}{\sqrt{h^2+k^2+l^2}} \tag{3.1}$$

The average crystallite size of bottom Mo thin films were measured using Scherer's formula [13]. The strain in the Mo thin films has been measured deposited at various DC power. The average crystallite size of Mo thin films deposited at various sputtered DC power (50, 100, 150, 200 W) are shown in Table 1. The average crystallite size is dependent on sputtered DC power. It has been found that with an increase in sputtered DC power average crystallite size increases. An increase in average crystallite size is due to the formation of larger and denser grain microstructure. There is a smaller number of voids with closed grain boundaries in Mo thin films. When sputtered DC power increases, the energy of sputtered atoms/ions of Mo also increases. This leads to forming dense microstructure morphology. There is a transformation of morphology such as pyramids, granular, fibrous, dendritic, etc., to large dense columnar morphology. An increase in sputtered DC power allows plasma ions to travel with high incident kinetic energy. These plasma ions create several nucleation sites and there is an increase in growth rate, which in turn increases the average crystallite size in the lateral direction. But on increasing further sputtered DC power, there is a decrease in average crystallite size. The effect of growth rate at different sputtered DC power (50, 100, 150, 200 W) are shown in Table 3.1.

Table 3.1: DC power-dependent Crystallite size and strain (%) of Mo thin films at room temperature.

Pressure	**10 mTorr**			**1 mTorr**			**10 and 1 mTorr**		
Power (W)	Crystallite Size (nm)	Strain (%)	Growth Rate (Å/s)	Crystallite Size (nm)	Strain (%)	Growth Rate (Å/s)	Crystallite Size (nm)	Strain (%)	Growth Rate (Å/s)
50	4.384	0.954	1.9	6.328	1.264	2.8	7.138	0.487	2.1
100	5.03	0.381	3.4	12.155	0.857	3.7	7.146	0.635	4.1
150	6.058	0.0953	6.5	13.196	0.54	5.4	9.591	0.381	5.6
200	6.089	0.381	8.6	9.646	0.54	9.3	12.06	0.635	8.4

3.3.2 Optical Reflectivity Analysis

For CIGS solar cell Mo layer acts as back ohmic contact with high reflectivity. Reflectivity is also an important factor for the qualitative analysis of Mo thin films. It serves as a back-ohmic contact that stores photon energy at which is used to enhance the performance of the CIGS solar cell. An increase in optical reflectivity is due to the increase in the surface quality of the Mo thin films. Ex-situ reflectivity of the Mo layer was measured using an in-house optical measurement setup automated with LabView 17.0 software. We have measured the ex-situ optical reflectivity of single layer Mo thin films deposited at various sputter power (50, 100, 150, 200 W). From Fig 3.2 (a) it was found that with an increase in sputter DC power the optical reflectivity increases. This means at pressure 10 mTorr with the increase of sputter power the crystallinity of Mo thin films increased. The average reflectance was 25.7-47.8 %. At lower pressure 1 mTorr, texture quality tends to improve which is shown in reflectivity spectra shown in Fig 3.2 (b). Here, the average reflectance has increased to 57.8-64.7

% [14]. This result is in accordance with researchers; they reported that at low deposition pressure Mo thin films exhibit good reflectance. Furthermore, the average reflectance of bilayer Mo thin films deposited at a pressure of 10 mTorr (bottom) and 1 mTorr (top) is found to be 63.0-66.7 % shown in Fig 3.2 (c). there is a fine marginal increment shift in optical reflectance. Optical reflectance in bilayer Mo thin films has been influenced by lower pressure deposition i. e. 1 mTorr. The high reflectivity of the Mo thin films increases the absorption in the absorber layer, which in turn helps to increase the efficiency of solar cells.

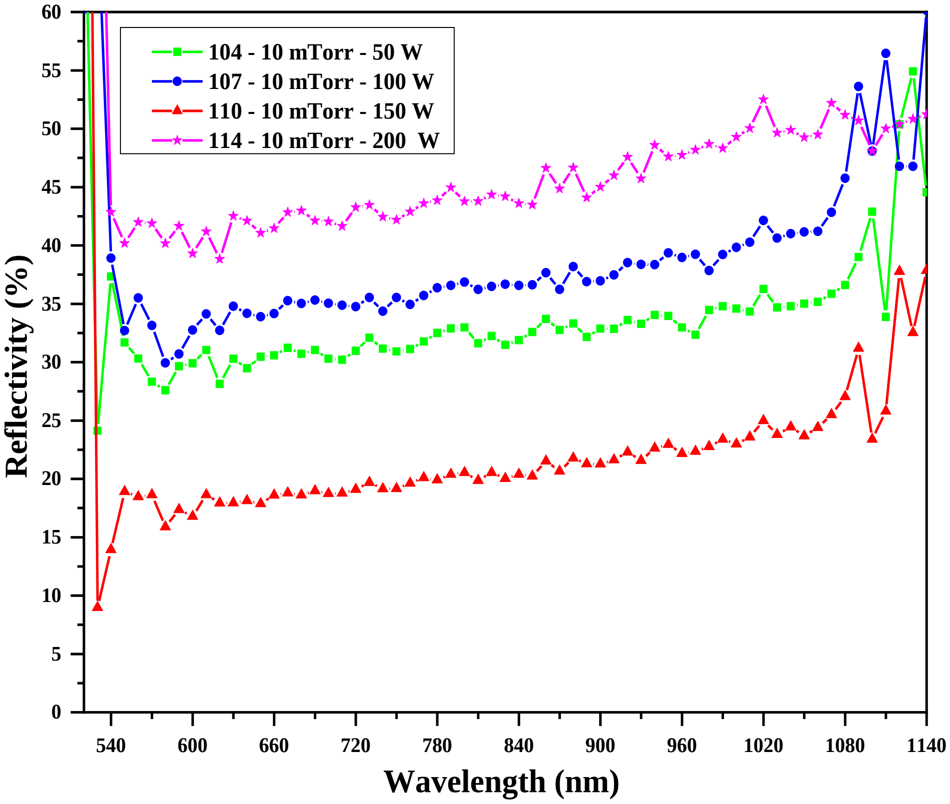

(a)

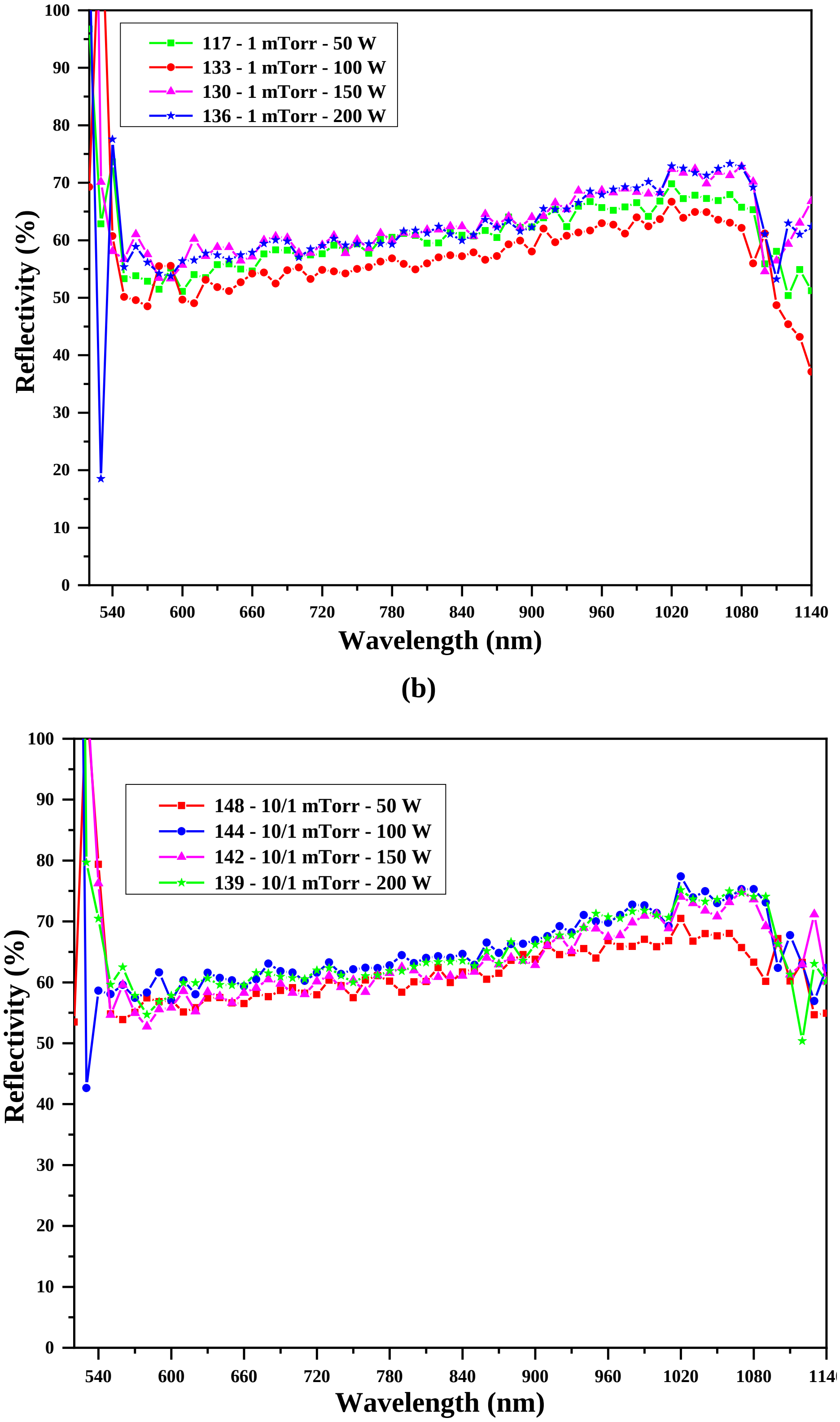

(b)

(c)

Fig 3.2: Reflectivity spectra of Mo thin films deposited at pressure (a) 10 mTorr and (b) 1 mTorr (top) and (c) 10 mTorr (bottom) and 1 mTorr (top).

3.3.3 Electrical Resistivity Analysis

The electrical resistivity of the Mo layer in the thin-film solar cell plays a prominent key role in the ohmic contact. The need for a back ohmic contact provides a non-rectifying electrical path to the absorbed photon between the back contact and the absorber layer. Single-layer Mo thin films deposited at high pressure are found to be highly resistive while those deposited at low pressure are low resistive thin films. Adhesion of low resistivity Mo thin film is poor contrary to high resistive Mo thin films. The bulk resistivity of Mo is 5.52 x 10^{-8} Ω-cm [2]. The sheet resistance of the single and bilayer Mo thin films has been measured by using a Four-point probe method. Table 3.2 represents the sheet resistance of single and bilayer layer Mo thin films deposited sputtered DC power (50, 100, 150, 200 W). From Table 3.2, it is concluded that with the increase of sputter DC power the resistivity of single layer Mo decreases. The sheet resistance of bilayer Mo thin film deposited at 150 W is (0.332 Ω/□). These results are in good agreement with reports [8]. The sheet resistance of Mo thin films is dependent on deposition parameters. Mo thin films deposited at high pressure and low deposition power do not favor low resistance. There is tensile stress in the Mo thin films with a greater number of grain boundaries and voids. Such thin films are porous in the microstructure. Mo thin films deposited at low pressure and high power have low resistivity. This is due to the large dense pack microstructure at high deposition power. Stack of different pressure has been incorporated for the deposition of bilayer Mo thin film. This helps to lower down electrical resistivity. There is an increase in grain size with lower deposition pressure. Reduction in sheet resistance of bilayer Mo thin films assists to decrease grain boundaries. There is a long pathway for Mo atoms to travel, due to which there is an increase in grain size and microstructure. Of course, a grain boundary is also one of the important key parameters for the low resistivity of Mo thin films.

Table 3.2: Sheet Resistance of Mo thin films at room temperature.

Sheet Resistance R_{sh} (Ω/□)			
Power (W)	**10 mTorr**	**1 mTorr**	**10 and 1 mTorr**
50	47.72	4.92	2.15
100	28.19	3.40	1.34
150	9.92	2.30	0.332

200	10.47	1.55	0.74

3.3.4 Atomic Force Microscopy Analysis

Surface texture is an informative tool that provides quantitative results regarding the growth of thin films. Surface texture and its modification in the thin film are directly affected by the deposition techniques and parameters such as pressure, power, substrate temperature, and thickness. AFM images of bilayer Mo thin films have been recorded using AFM-Keysight 5500 Scanning Probe Microscope (Mode-ACAFM). The topographical view of Mo thin films describes the growth of grain in the lateral direction. Sputtering power and deposition pressure affect the substantial growth in the preferred direction of Mo thin films. The kinetic energy of the sputtered atoms at dc sputtering power increases, mean free path of Mo atoms at working pressure assists to form the nucleation site. At 50 W DC power, uneven small Mo mounds have been formed shown in Fig. 3.3 (a and b). Incoming Mo atoms have low kinetic energy due to which non-uniform surface texture formed with surface roughness Rrms 15.633 nm. On increasing DC power to 100 W, surface texture comprises of agglutinated columnar rods and globules of Mo atoms was observed shown in Fig. 3.3 (c and d). Surface roughness Rrms increased to 37.123 nm. Due to the presence of mixed texture (columnar rods and globules), surface roughness increased. At 150 W and 200 W DC power, the Mo atom forms a homologous dense compact structure [15]. The crystallite size was enhanced due to the nucleation of Mo atoms arriving with high kinetic energy at the substrate. Mo atoms sublimate into a continuous prolate spheroid structure. This decreases surface roughness to Rrms 17.893 nm. Further, the coalescence of the Mo atom reduces grain boundary, as well as porous structure. This helps to change the porous structure into the dense structure at 150 W shown in Fig. 3.3 (e and f). This results in low resistivity too. But at 200 W, the size of the prolate spheroid structure of Mo atoms increases and forms crystallites with a bigger size shown in Fig. 3.3 (e and f). Surface roughness Rrms value increased to 24.947 nm leading to an increase in resistivity too. These results are good in agreement to compare to [16].

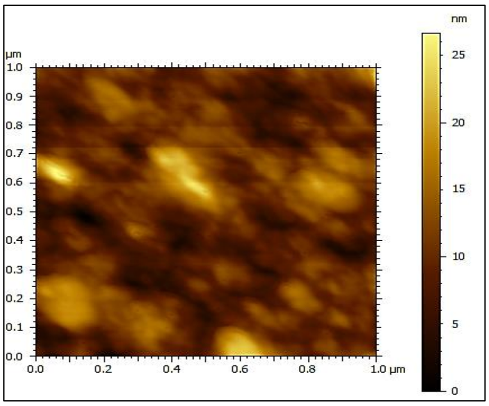
nm
µm
1.0
0.9
0.8
0.7
0.6
0.5
0.4
0.3
0.2
0.1
0.0
0.0
0.2
0.4
0.6
0.8
1.0 µm
25
20
15
10
5
0

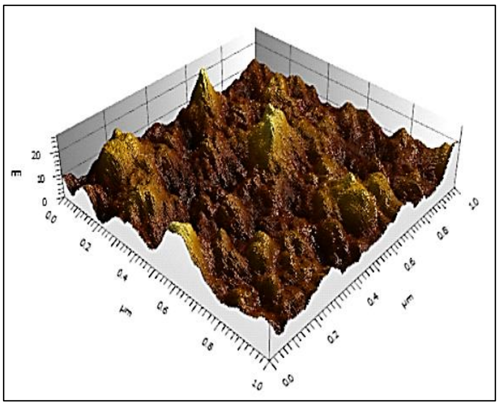
20
15
0
nm
µm
µm

(a) **(b)**

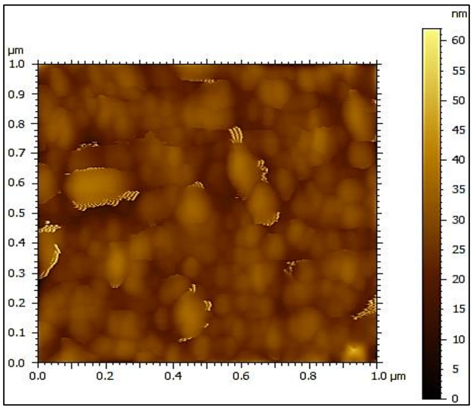
nm
µm
1.0
0.9
0.8
0.7
0.6
0.5
0.4
0.3
0.2
0.1
0.0
0.0
0.2
0.4
0.6
0.8
1.0 µm
60
55
50
45
40
35
30
25
20
15
10
5
0

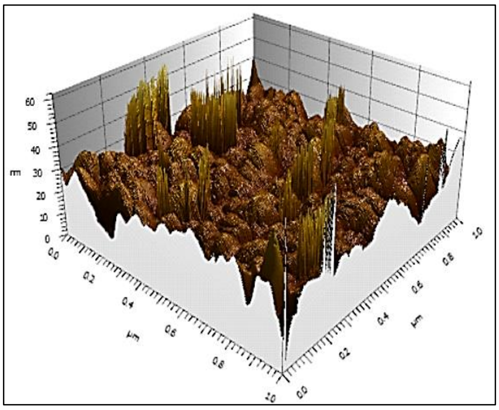
60
50
40
30
20
10
0
nm
µm
µm

(c) **(d)**

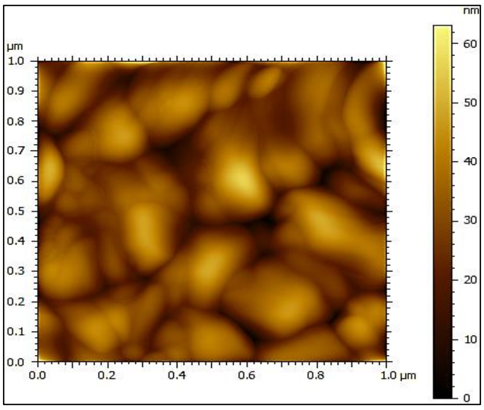
nm
µm
1.0
0.9
0.8
0.7
0.6
0.5
0.4
0.3
0.2
0.1
0.0
0.0
0.2
0.4
0.6
0.8
1.0 µm
60
50
40
30
20
10
0

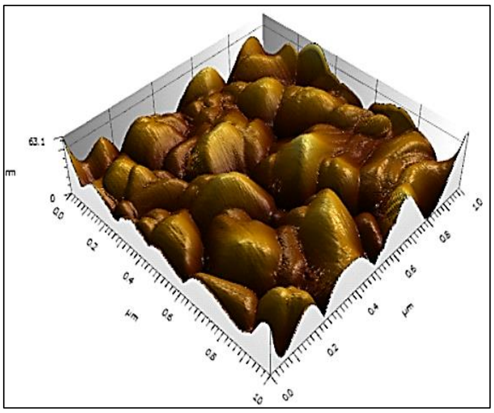
63.1
nm
0
µm
µm

(e) **(f)**

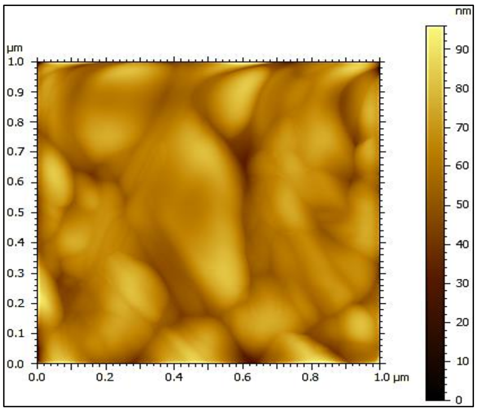
nm
µm
1.0
0.9
0.8
0.7
0.6
0.5
0.4
0.3
0.2
0.1
0.0
0.0
0.2
0.4
0.6
0.8
1.0 µm
90
80
70
60
50
40
30
20
10
0

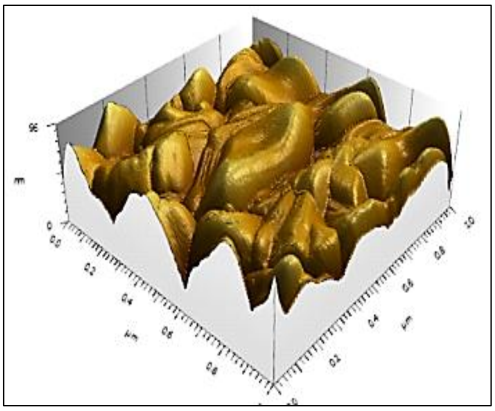
96
nm
µm
µm

(g) **(h)**

Fig 3.3: AFM images (a, c, e, g) 2D view and (b, d, f, g) 3D view of bilayer Mo thin films deposited at sputter power (a, b) 50 W, (c, d) 100 W, (e, f) 150 W and (g, h) 200 W.

3.3.5 Scanning Electron Microscopy Analysis

The top and a cross-sectional view of bilayer Mo thin films deposited at different sputter power give information about the microstructure of the Mo thin films. Fig. 3.4 represents the top and cross-sectional view of bilayer Mo thin films deposited at 10 mTorr (bottom) and 1 mTorr (top) having sputter power (50, 100, 150, 200) W at approximately with the substrate at RT. Scanning Electron Microscopy of bilayer Mo thin films provides information regarding porosity or void in the microstructure. The grain growth of Mo thin films was affected by the sputter power. At low sputter power, Mo adatoms have less kinetic energy, due to which porous and uneven crystal grows. From the images, it has been noticed that Mo thin films have a tightly dense pack microstructure. From the cross-sectional view of bilayer Mo thin films, it has been found that the thickness of the Mo thin films is 1 μm with columnar or dendritic microstructure [17, 18].

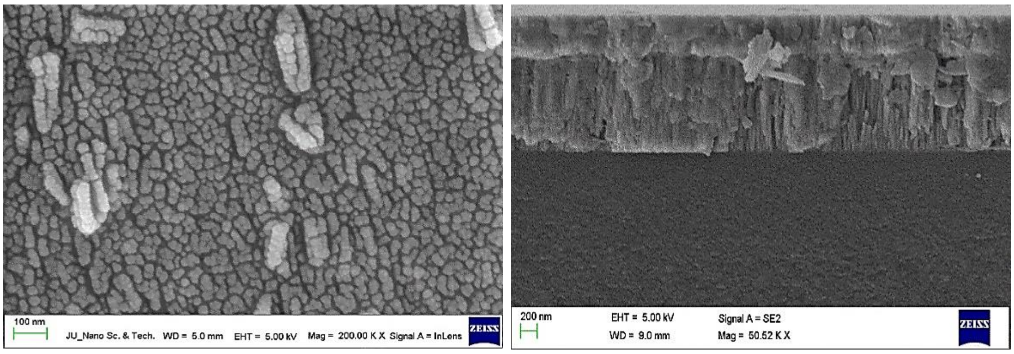

(a) **(b)**

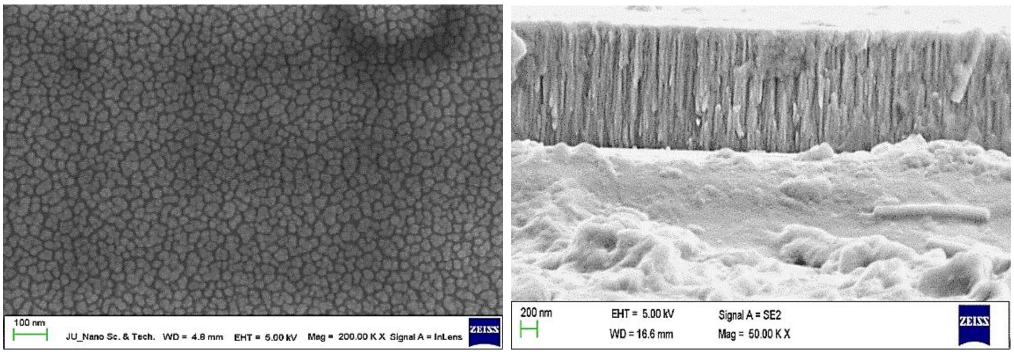

(c) (d)

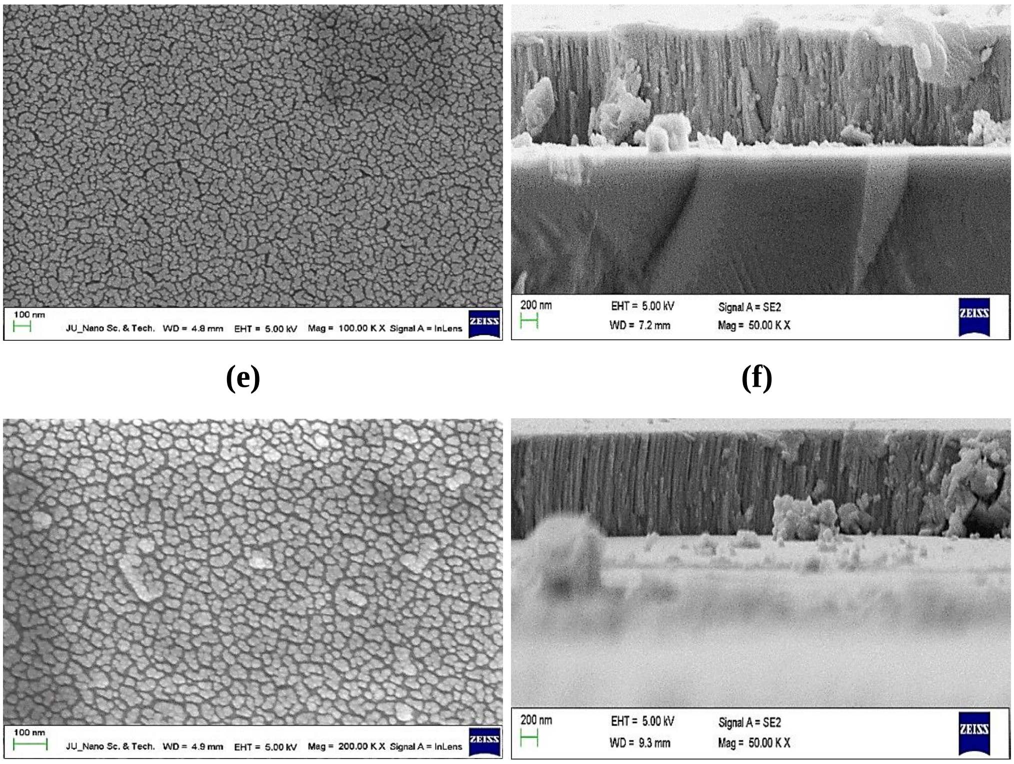

(e) (f)

(g) (h)

Fig. 3.4. SEM images (a, c, e, g) top view and (b, d, f, g) cross-sectional view of bilayer Mo thin films deposited at sputter power (a, b) 50 W, (c, d) 100 W, (e, f) 150 W and (g, h) 200 W.

The top and cross-sectional images of bilayer Mo thin films reveal the formation of islands, nuclei, coalescence, and clusters. There is a tendency to form island structure on the substrate surface during the deposition process which is dependent on (a) High substrate temperature, (b) Low boiling point of film elements, (c) Low deposition rate, (d) Weak binding forces between substrate and thin film, (e) High surface energy of thin-film material and low surface energy of the substrate. Initially, Mo adatoms have high surface energy as these atoms were sputtered out with high voltage from the cathode surface; island structures have formed, which unites to form nuclei at the surface of the substrate by lowering their surface energy. These nuclei at the substrate surface form a critical nucleus, which has critical size and conglomerate to form a continuous thin film. Bilayer Mo thin films deposited at RT have a linear increase in growth microstructure with varied sputter power. In Fig. 3.4 (a) top view image of bilayer Mo thin film deposited at 50 W reports the uneven particle shape in addition to it, sporadic agglomeration of Mo adatoms have developed while in Fig. 3.4 (b), a cross-sectional image shows an uneven porous columnar growth. The vertical view shows the presence of the agglomeration of Mo adatoms. Both top and layer have visible separation at their interface. As the sputter power rises to 100 W, gradual structure changes occur, the uneven particles start to get into a spherical shape. There is a nucleation barrier during the growth process, which, leads to forming grain boundaries. The columnar growth has a height difference between the top layer and bottom layer. There is a mismatch in the orientation of columnar growth of the top and bottom layers. Fig. 3.4 (c) and (d) show the microstructural image of bilayer Mo thin film deposited at 100 W. Further, the top view in Fig. 3.4 (e) shows the formation of a granular nature. V-shape structure in columnar growth has been noticed in the cross-sectional image of bilayer Mo thin films deposited at 150 W shown in Fig. 3.4 (f). It has columnar growth with broadening of columnar grains. The grains have grown more in size as they unite to form compact dense structure. There is a complete transition from porous to the compact dense microstructure of Mo thin films. From top view images, it has been predicted that columns may be isolated with a very fine edge difference. This could help some amount of Na from glass substrate to travel through it, which enhances the performance of the CIGS solar cell. At 200 W sputter power, the vertical orientation of Mo thin film has grown to have elongated columns in morphology structure. This is evident from Fig. 3.4 (g) and (h). Some uneven agglomeration of Mo atoms is found on the film surface. Here grain boundaries are more pronounced, which may change towards porous structure, and electrical resistivity increases.

3.4 Influence of Substrate temperature

Substrate temperature affects the growth kinetics of material. Here we have studied the effect of substrate temperature on single and bilayer Mo thin films deposited. Single-layer Mo thin films at 10 and 1 mTorr while bilayer Mo thin films bottom layer with pressure 10 mTorr and the top layer with pressure 1mTorr had been deposit. DC power was upheld to (50, 100, 150, 200 Watt) approximately. The substrate temperature was maintained to 215 ˚C. Phase detection, reflectivity, morphology, and electrical properties of Mo thin films were investigated.

3.4.1 X-Ray Diffraction Analysis

All Mo thin films show the tendency to form a cubic crystal structure with phase (110) in the C-axis plane. X-ray diffraction analysis results were confirmed with the JCPDS card (42-1102) shown in Fig. 3.5 (a), (b), and (c). Due to substrate temperature intensity of major peak and FWHM varied. The major peak was found at 40.1 ˚ with (h k l) values (110) [19]. At high pressure of 10 mTorr and low deposition power 50 W, single Mo thin film has very low intensity and broad FWHM. The energy of impinging Mo adatoms in the presence of substrate temperature and high pressure was not enough to form a cubic crystal structure. The surface mobility of incoming adatoms was low due to which they could not able to physically adsorb on the surface of the substrate. As the deposition power increase, the cubic crystallography of Mo thin film was more enhanced. At deposition power 150 W, Mo adatoms have minimum surface mobility and enough surface diffusion energy to arrange themselves well in a cubic structure. Further, on increasing sputtering power incoming Mo adatoms could not be able to lose their kinetic energy due to very high surface mobility at the substrate surface and become unstable due to which cubic structure was not well-formed. There was a lattice misfit between Mo thin film and substrate. At lower pressure i. e., 1 mTorr, the XRD peak was more intense due to low collision and high mean free path of Mo adatoms. This helps Mo adatoms to adhere well to substrate with a high deposition rate. Another minor peak at 70.2 ˚C was also found but still, the intensity and FWHM were not affected by the presence of substrate temperature compared to RT. The bilayer Mo thin film also has both major and minor peaks like that present in a single layer Mo thin film deposited at 1 mTorr. The intensity and sharpness of major peaks were increased as well as FWHM decreased. This is due to the improved crystallinity of Mo atoms to well adhere to the substrate and there is an increase in grain size due to an increase in thickness. The intensity of minor peaks was reduced because of deposition of the bottom layer at high pressure 10 mTorr. The growth rate and presence of substrate temperature 215 ˚C affect crystallite size and strain. These results have been mentioned in Table 3.3.

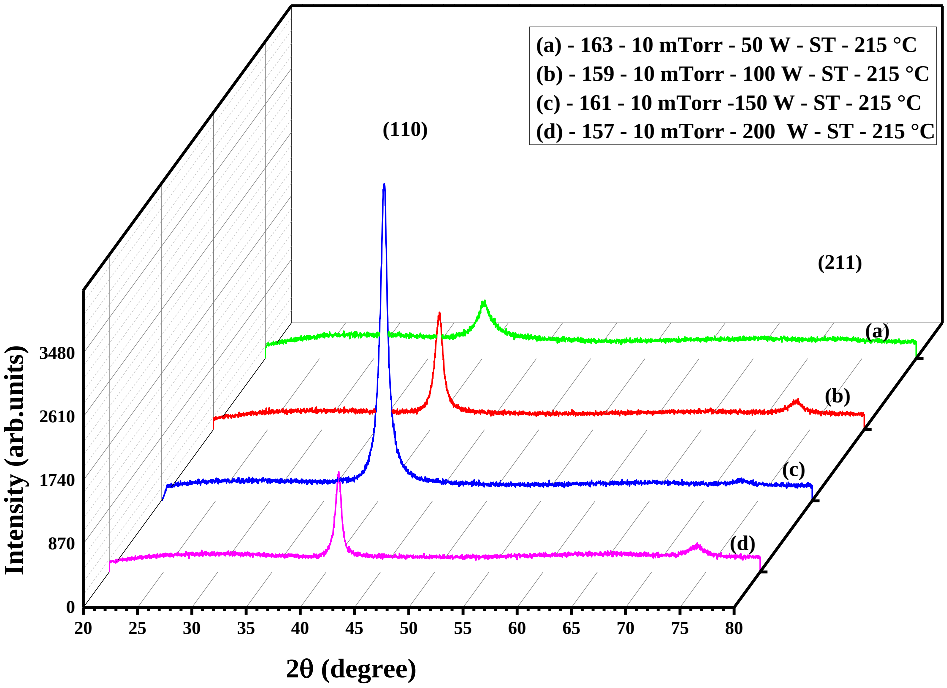

(a)

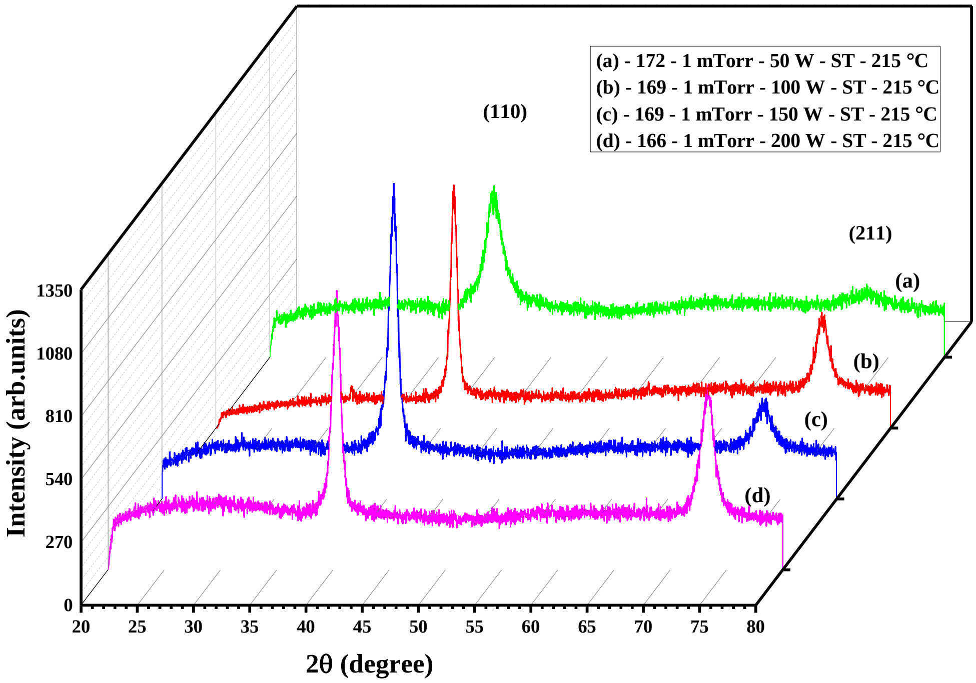

(b)

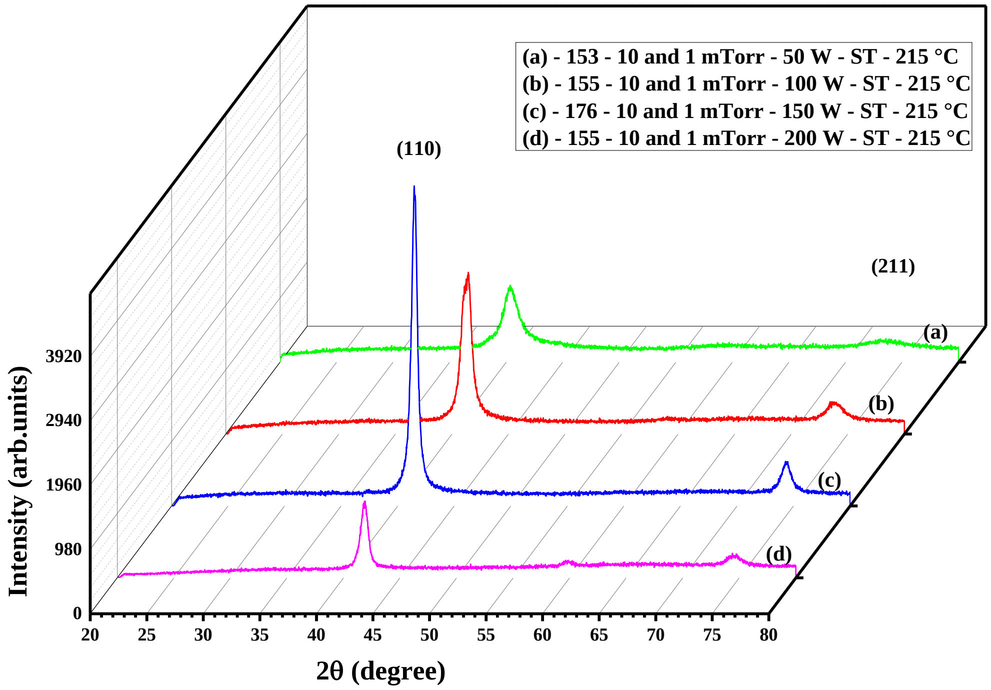

(c)

Fig. 3.5: XRD analysis of Mo thin films deposited at (a) 10 mTorr, (b) 1mTorr, and (c) 10 mTorr (bottom) and 1 mTorr (Top) at ST 215 ˚C with different DC power.

Table 3.3: Crystallite size and strain (%) of Mo thin films at the substrate temperature of 215 ˚C.

Pressure	**10 mTorr**			**1 mTorr**			**10 and 1 mTorr**		
Power	Crystallite Size (nm)	Strain (%)	Growth Rate (Å/s)	Crystallite Size (nm)	Strain (%)	Growth Rate (Å/s)	Crystallite Size (nm)	Strain (%)	Growth Rate (Å/s)
50 W	3.012	0.942	1.2	4.652	0.589	1.9	5.404	2	2.1
100 W	7.047	0.953	3.2	10.423	0.635	4.3	10.788	0.953	3.8
150 W	11.689	0.635	5.5	11.68	0.634	6.0	10.219	0.635	5.2
200 W	8.758	0.635	8.4	11.262	0.635	7.4	11.874	0.381	8.3

3.4.2 Optical Reflectivity Analysis

Optical reflectivity of single and bilayer Mo thin film was affected by substrate temperature 215 ˚C compared to room temperature. The optical reflectivity of single and bilayer Mo thin films at substrate temperature 215 ˚C is shown in Fig. 3.6 (a), (b), and (c). Optical reflectivity of Mo thin films at substrate temperature 215 ˚C was found 35 ± 5 % at high pressure (10 mTorr) and 55 ± 5 % for low pressure (1 mTorr) Mo thin films. There was no discrete change in optical reflectivity of single layer Mo thin films at variable deposition power in the presence of substrate temperature. The substantial effect in the increment of optical reflectivity was noticed with the increase of deposition power in bilayer Mo thin films. From 50 ± 2 % to 70 ± 3 % optical reflectivity increased due to an increase in deposition power 50 to 200 W.

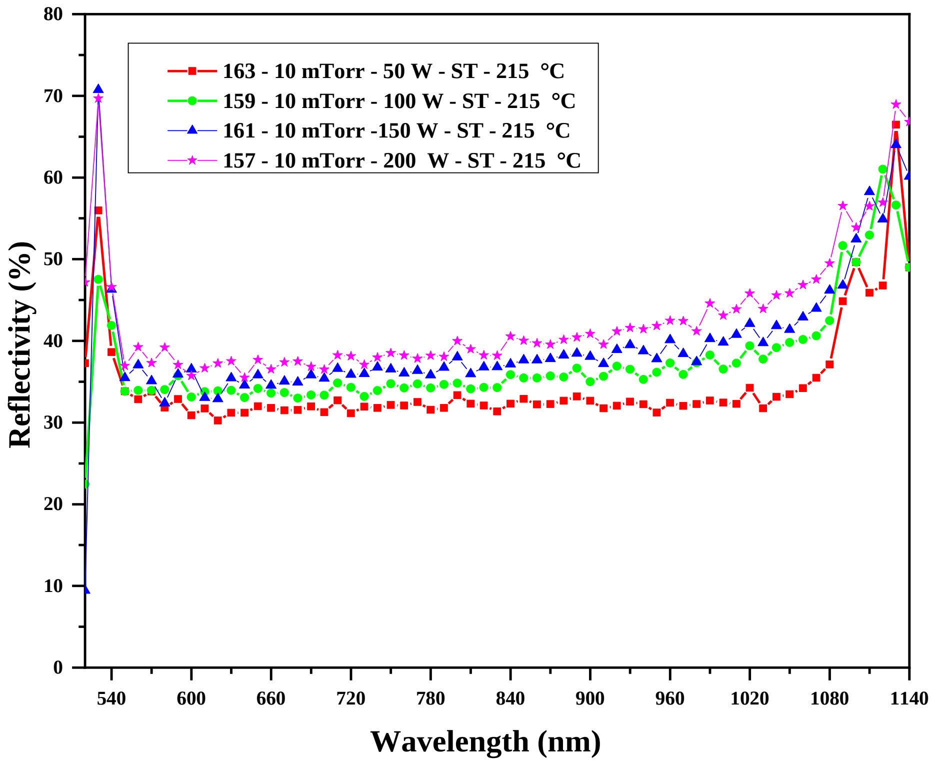

(a)

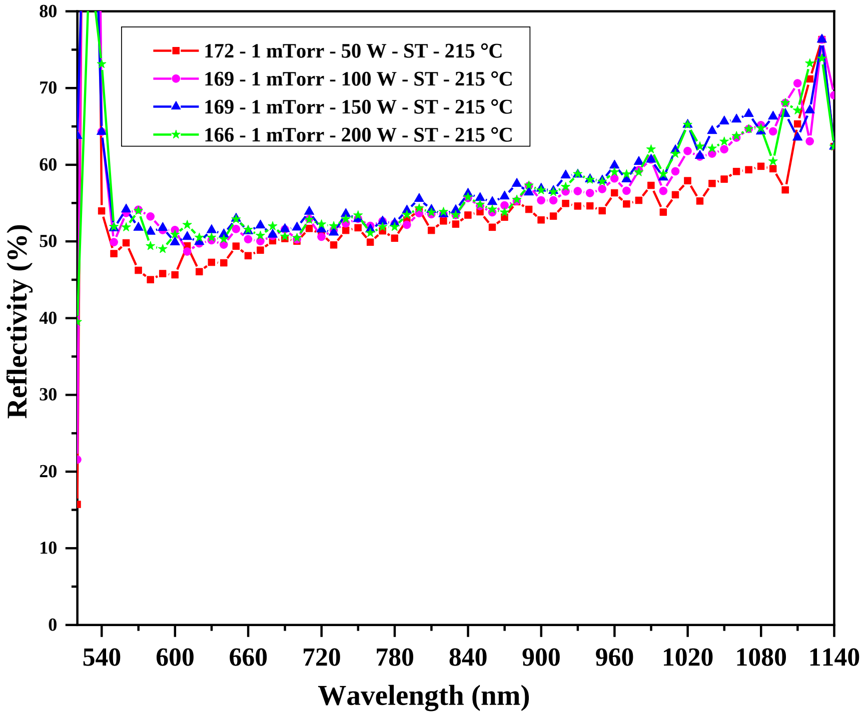

(b)

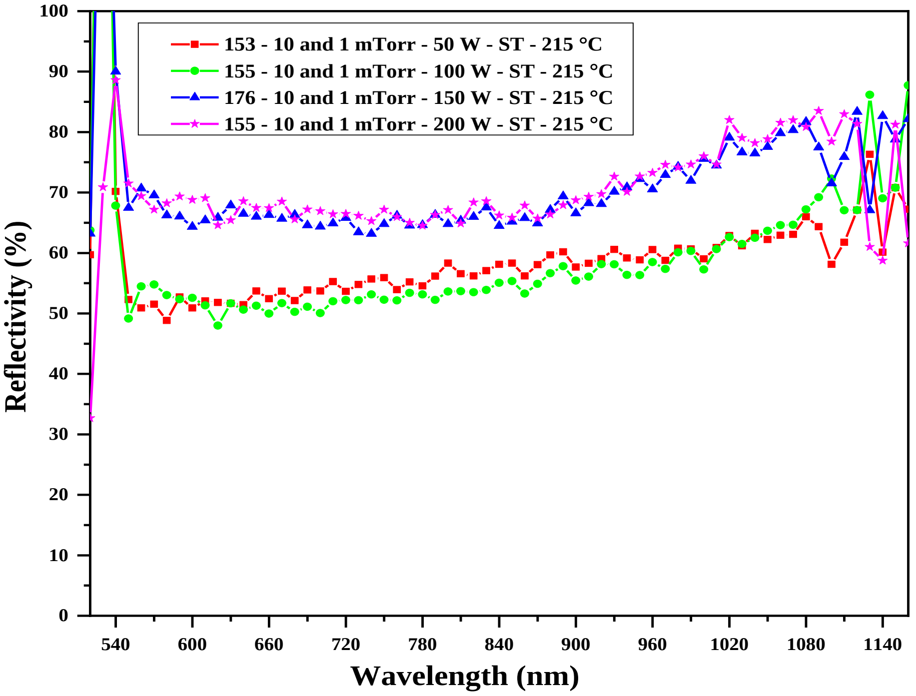

(c)

Fig. 3.6: Reflectivity spectra of Mo thin films deposited at pressure (a) 10 mTorr and (b) 1 mTorr (top) and (c) 10 mTorr (bottom) and 1 mTorr (top) ST 215 ˚C with different DC power.

3.4.3 Electrical Resistivity Analysis

Electrical resistivity is affected by vacancies, grain boundaries, interstitial atoms, impurities, and temperature. Influence of substrate temperature 215 ˚C on electrical resistivity/sheet resistance of single and bilayer Mo thin film in Table 3.4. There is not much change in sheet resistance of Mo thin film compared to room temperature. The lowest sheet resistance was 0.57 Ω/□ for bilayer Mo thin film deposited at 150 W [20].

Table 3.4: Sheet Resistance of Mo thin films at Substrate Temperature 215 ˚C.

Sheet Resistance R_{sh} (Ω/□)			
Power (W)	**10 mTorr**	**1 mTorr**	**10 and 1 mTorr**
50	50.75	5.81	2.48
100	12.33	1.45	0.97
150	10.96	1.96	0.57
200	4.51	9.08	0.74

3.4.4 Atomic Force Microscopy Analysis

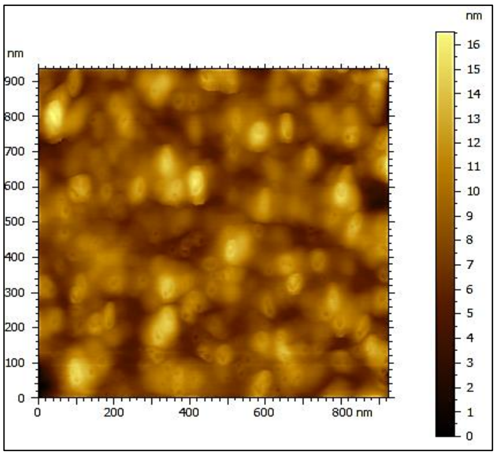

(a)

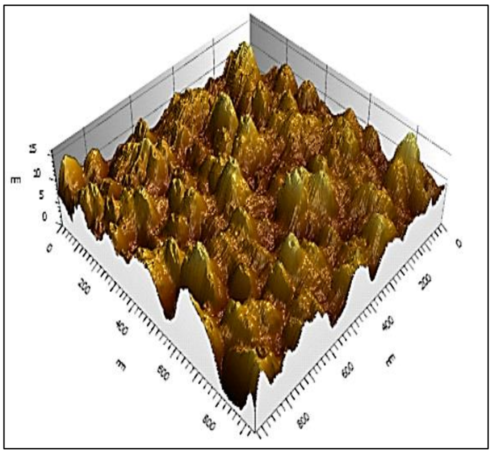

(b)

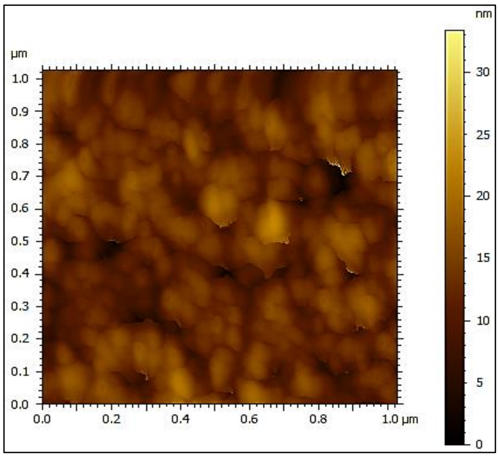

(c)

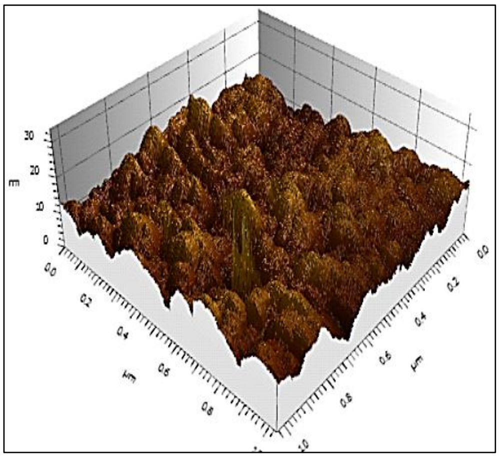

(d)

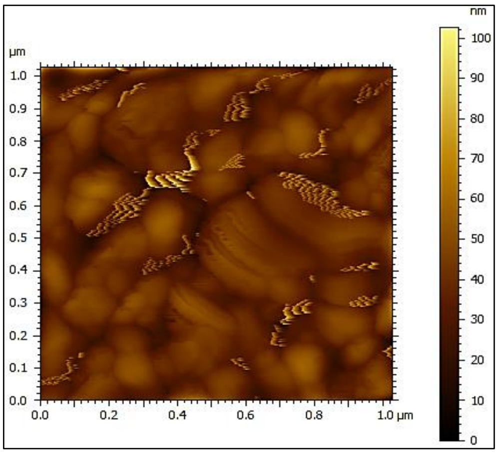

(e)

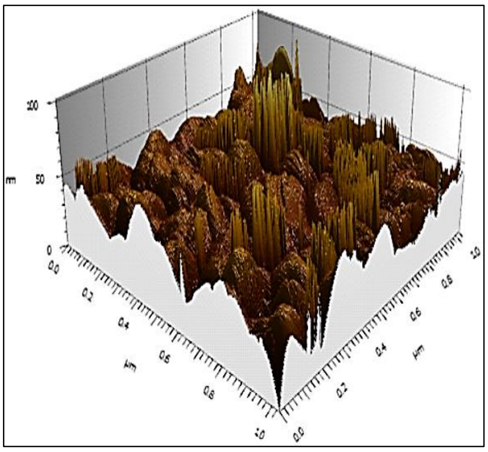

(f)

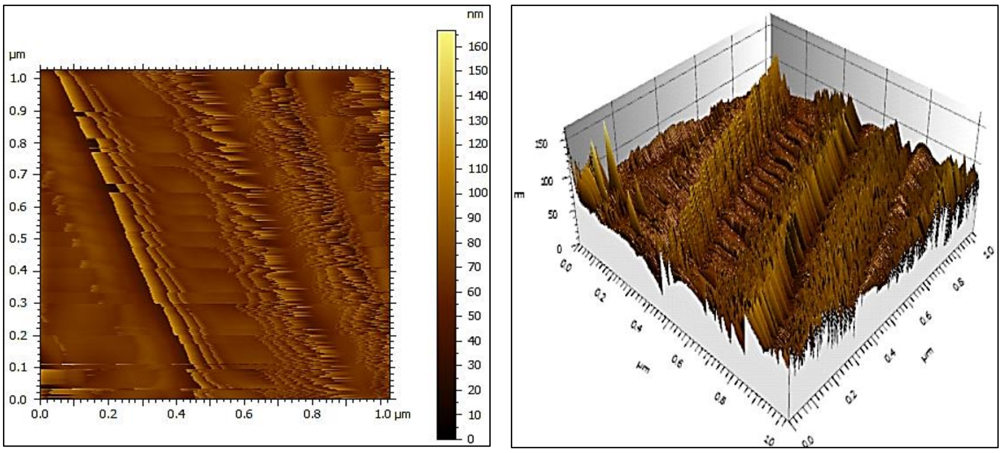

(g) (h)

Fig. 3.7: AFM images 2D (a, c, e, g) view and 3D (b, d, f, g) view of bilayer Mo thin films deposited at ST 215 ˚C with sputter power (a, b) 50 W, (c, d) 100 W, (e, f) 150 W and (g, h) 200 W.

Substrate temperature 215 ˚C has an impact on the surface texture of bilayer Mo thin films [21, 22]. Above Fig. 3.7 represents the surface texture of bilayer Mo thin films deposited at variable DC power. At 50 W DC power, Mo thin film has a similar texture to Mo thin film deposited at room temperature. It has tapered mounds texture but slightly are unevenly grown surface due to which surface roughness is 27.165 nm shown in Fig. 3.7 (a and b). All Mo atoms tend to form dense circular texture which reduces surface roughness to 6.079 nm shown in Fig. 3.7 (c and d). Here homogenous texture of Mo thin film was observed. On increasing DC power to 150 W, columnar rods are surrounded by uneven circular Mo crystallites shown in Fig. 3.7 (e and f). Due to the presence of both columnar and circular texture surface roughness increase to 14.667 nm. The thick wall of Mo columnar rods has been formed at distance apart from each other when DC power increased to 200 W. Columnar rods are not densely packed; they form porous structure and increase in resistivity too, as shown in Fig. 3.7 (g and h).

3.4.5 Scanning Electron Microscopy Analysis

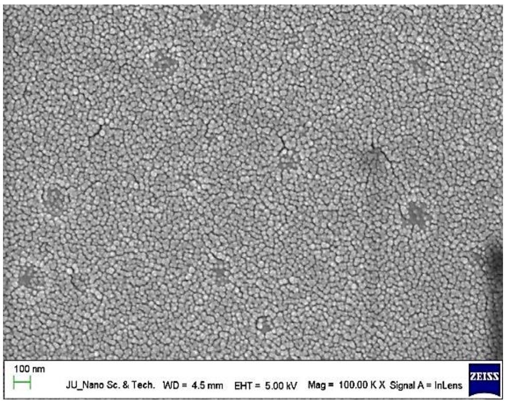
100 nm
JU_Nano Sc. & Tech. WD = 4.5 mm EHT = 5.00 kV Mag = 100.00 K X Signal A = InLens
ZEISS

(a)

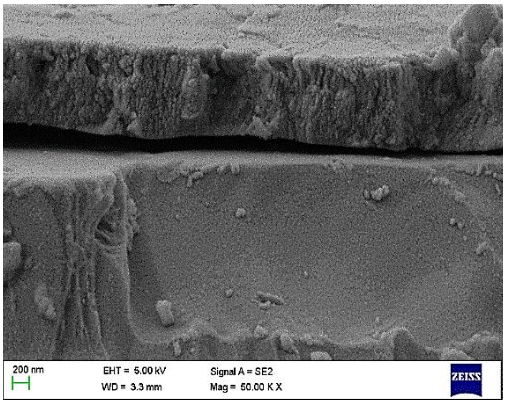
200 nm
EHT = 5.00 kV
WD = 3.3 mm
Signal A = SE2
Mag = 50.00 K X
ZEISS

(b)

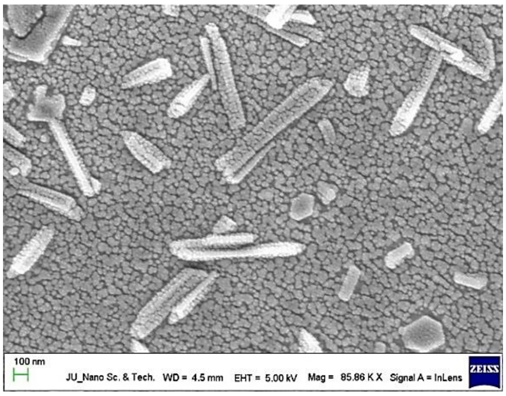
100 nm
JU_Nano Sc. & Tech. WD = 4.5 mm EHT = 5.00 kV Mag = 85.86 K X Signal A = InLens
ZEISS

(c)

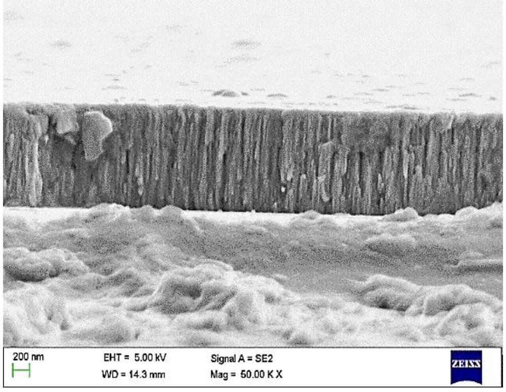
200 nm
EHT = 5.00 kV
WD = 14.3 mm
Signal A = SE2
Mag = 50.00 K X
ZEISS

(d)

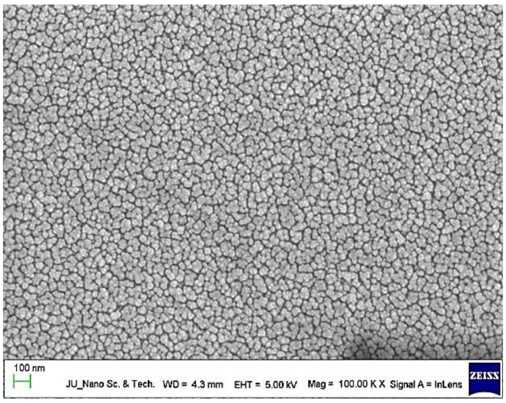
100 nm
JU_Nano Sc. & Tech. WD = 4.3 mm EHT = 5.00 kV Mag = 100.00 K X Signal A = InLens
ZEISS

(e)

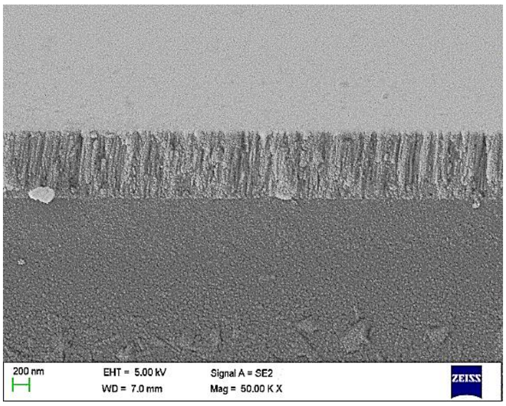
200 nm
EHT = 5.00 kV
WD = 7.0 mm
Signal A = SE2
Mag = 50.00 K X
ZEISS

(f)

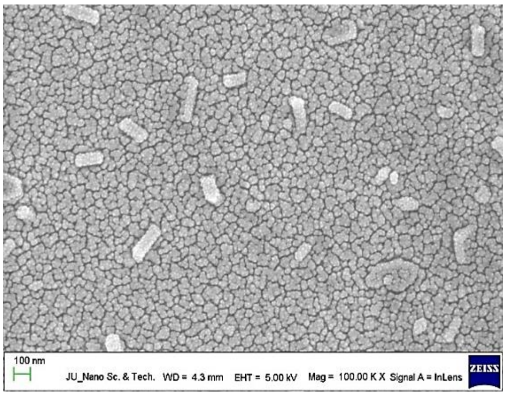
100 nm
JU_Nano Sc. & Tech. WD = 4.3 mm EHT = 5.00 kV Mag = 100.00 K X Signal A = InLens
ZEISS

(g)

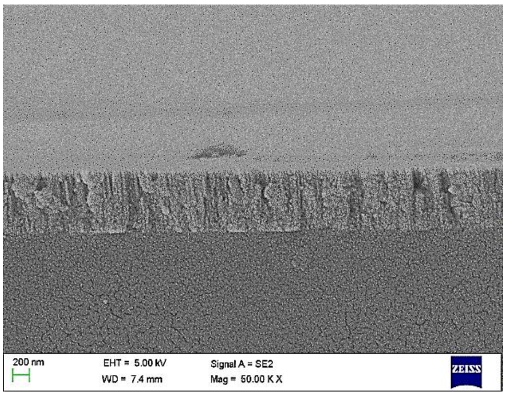
200 nm
EHT = 5.00 kV
WD = 7.4 mm
Signal A = SE2
Mag = 50.00 K X
ZEISS

(h)

Fig. 3.8: SEM images (a, c, e, g) top view and (b, d, f, g) cross-sectional view of bilayer Mo thin films deposited at ST 215 ˚C with sputter power (a, b) 50 W, (c, d) 100 W, (e, f) 150 W and (g, h) 200 W.

Mo adatoms sputtered at deposition power 50 W, kinetic energy was not enough for all Mo adatoms to cross the thermal barrier at the substrate surface due to substrate temperature 215 ˚C. Fig. 3.8 (a) and (b) show top and cross-sectional SEM images of bilayer Mo thin film deposited at 50 W. In the top view image, the deep craters, voids, and cracks on the surface were observed. At 1 mTorr Mo adatoms have high energy to hit the Mo film surface formed at high pressure. A cross-sectional image shows that the Mo layer was not well adhered to the substrate. Even partly top surface can be viewed which is uneven with thickness. Fig. 3.8 (c) and (d) show SEM images for bilayer Mo thin film deposited at 100 W. Mo adatoms have enough kinetic energy to reach the surface substrate and lose their surface mobility and get adhere to the substrate. From an image Fig. 3.8 (c), the seed layer or bottom layer at high pressure 10 mTorr forms a homogenous layer but layer with low pressure 1 mTorr forms big clusters. The energy of incoming Mo adatoms and the presence of thermal energy at the substrate surface allows atoms to reunite to form clusters rather than diffusing in the bottom layer to form the homogenous film [19, 23]. Stranski-Krastanov growth mode has been followed by Mo adatoms. Cross-sectional image (d) shows the formation of uneven columnar grain and surface has small bulgy bumps. The dense columnar growth of Mo bilayer has been found at power 150 W as shown in Fig. 3.8 (e) and (f). There is surface diffusion of Mo adatoms with pressure 1 mTorr to Mo bottom layer. Even no fine edge separation is present in bilayer Mo thin film. Both top and cross-sectional images represent the fine homogeneity thin film which leads to Frank-Van der Merwe growth mode in the presence of substrate temperature 215 ˚C. On increasing sputter power to 200 W, again small islands have formed on the top surface. There is an incomplete formation of nuclei and coalescence processes of incoming Mo adatoms at the substrate surface. Partially atoms are diffused to the bottom layer at 200 W power. There is the possibility of scattering or reflection of incoming Mo adatoms at the substrate surface. The high kinetic energy of incoming Mo adatoms and thermal energy at the substrate surface does not allow adatoms to minimize their surface energy and diffuse to partially grown film. Small islands and uneven columnar growth with some porous voids can be viewed in Fig. 3.8 (g) and (h).

3.5 Bilayer Molybdenum thin film at Different Thickness

3.5.1 X-Ray Diffraction Analysis

Crystallographic cubic phase with (h k l) values (110) and (211) at 2θ values 40.2˚ and 73.9 ˚ was found on performing X-Ray diffraction (Bragg-Brentano geometry) analysis of all bilayer Mo thin films. JCPDS card (01-1208) [19] data was used to confirm the XRD analysis data. Bilayer Mo thin films were deposited at 150 W DC power. The major peak of bilayer Mo thin film with thickness 300 nm as shown in Fig. 3.9 (a) was less intense and have broad FWHM compared to Mo 500 nm and Mo 1000 nm as shown in Fig. 3.9 (a), (b). The major peak of Mo 500 nm and Mo 1000 nm are similar, slightly FWHM of Mo 1000 nm is less. The crystallinity of Mo 1000 nm improves due to the increase in thickness with the presence of sharp major and minor peaks shown in Fig. 3.9 (c). Structure evolution in Mo thin films takes place with an increase in thickness. In Mo 300 nm small crystallites are randomly oriented along (110) and (211) plane in the early and later growth stage while Mo 500 nm and Mo 1000 nm have preferred orientation in the plane. Mo 500 nm does not have crystallite growth in the (211) plane because it does not have crystallites gown in any random direction. Coalescence of isolated crystallites in early and later stages of growth is free of grain boundaries and leads to a coarse dense pack structure. The surface energy of crystallites grown in the (110) plane is more than the (211) plane. The homogenous film growth process is the result of the minimization of the surface energy of individual grain in a preferred orientation. In the presence of ST-215 ˚C, incoming Mo species have enough kinetic energy to coalescence at the surface of the substrate rather than scattering. Mo species accelerate with high velocity and reach substrate surface but later under equilibrium thermodynamic conditions, they reduce their free surface energy and nucleation process initiates followed by all growth states and finally, conformal growth of Mo thin film occurs.

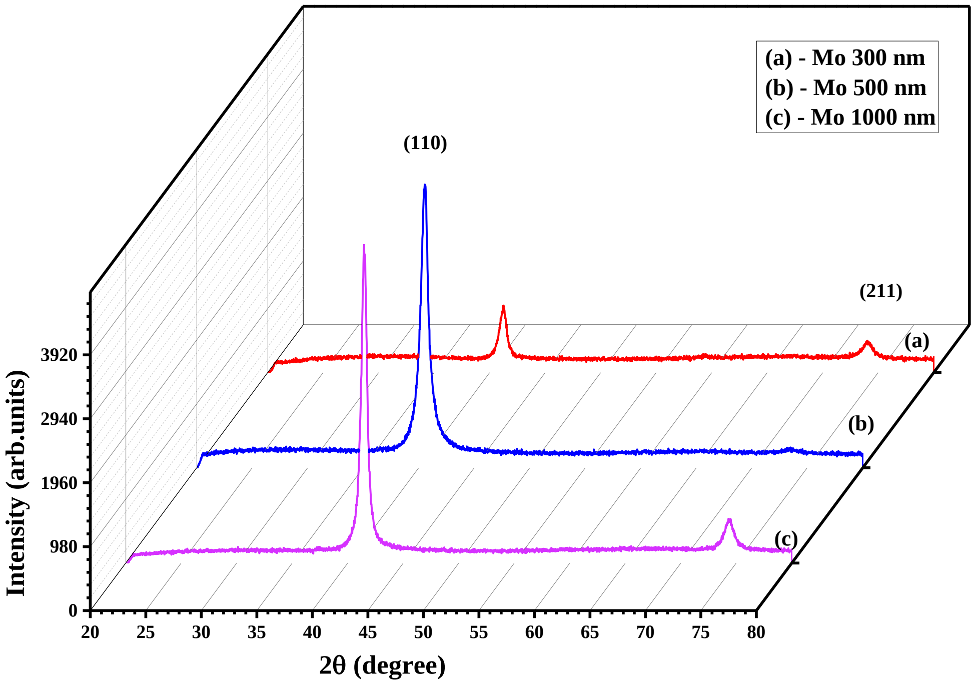

Fig. 3.9: XRD analysis of bilayer Mo thin films with a thickness of (a) 300 nm, (b) 500 nm, and (c) 1000 nm.

3.5.2 Optical Reflectivity Analysis

For back ohmic contact of CIGS solar cells, the high reflectivity of back contact is more favorable. Fig. 3.10 represents the optical reflectivity of bilayer Mo 300 nm, Mo 500 nm, and Mo 1000 nm. More thickness leads to the high reflectivity of bilayer Mo thin films, due to multiple internal reflections from multiple planes. Surface roughness, opaqueness, and deposition conditions also contribute to the reflectivity of metallic films. Metallic films tend to emit visible energies after filling unoccupied energy levels on absorbing photons of visible range. The average reflectance is 68 % for Mo 500 nm and Mo 1000 nm, but it is half for Mo 300 nm [24].

3.5.3 Electrical Resistivity Analysis

Low electrical resistivity with optimum reduced thickness is always desirable for ohmic back contact. Not only vacancies, grain boundaries, impurities, and temperature but lateral growth of the Mo layer affects the electrical properties. Assessment of Mo layer deposited with different thickness under the influence

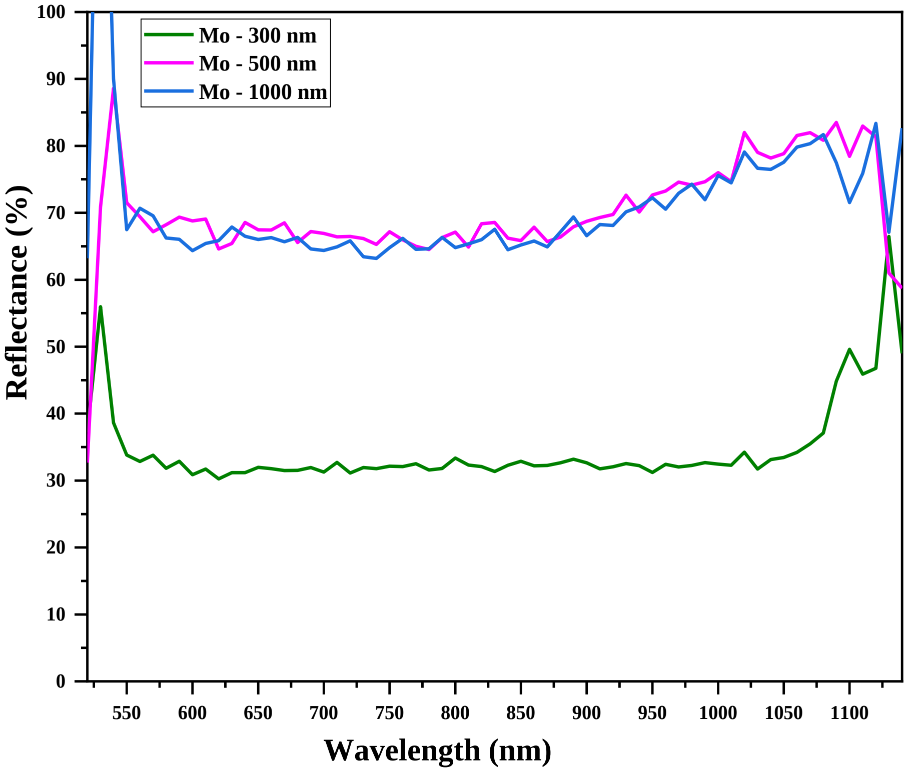

Fig. 3.10: Optical reflectivity of bilayer Mo thin films with a thickness of 300 nm, 500 nm, and 1000 nm.

of substrate temperature is carried out. Influence of substrate temperature 215 ˚C on sheet resistance of single and bilayer Mo thin film in Table 3.5. There is not much change in sheet resistance of Mo thin film compared to room temperature. The lowest sheet resistance was 0.52 Ω/□ for bilayer Mo thin film deposited at 150 W [8].

Table 3.5: Sheet Resistance and Crystallite size of bilayer Mo thin films for different thicknesses.

Sample (nm)	Sheet Resistance Rsh (Ω / □)	FWHM (˚)	Crystallite Size (nm)
Mo 300	2.03	1.341	6.62
Mo 500	0.68	0.824	10.74
Mo 1000	0.52	0.725	12.24

3.5.4 Scanning Electron Microscopy Analysis

Columnar crystallite Mo structure has grown in the presence of substrate temperature ST-215 ˚C. Fig. 3.11 contains cross-sectional and top view images of Scanning Electron Microscopy of bilayer Mo 300 nm, Mo 500 nm, and Mo 1000 nm. Mo 300 nm have columns partly with unequal size and shape as shown in Fig. 3.11 (a) compared to Mo 500 nm and Mo 1000 nm. The very fine closed dense dendric microstructure was observed in Mo 500 nm film as shown in Fig. 3.11 (c). A subtle difference in Mo 500 nm column has also been noticed which may be due to the difference in deposition pressure. Slight wide columns as shown in Fig. 3.11 (e) appeared for Mo 1000 nm; the top layer (1 mTorr) is completely diffuse into the bottom layer (10 mTorr) forming a continuous column with an inseparable column edge difference. The top view of all three bilayers in Fig. 3.11 (b), (d), and (f) depict how the difference in thickness affects grain size and agglomeration of Mo adatoms in the presence of ST 215 ˚C. Cluster formation and grain size ameliorate for Mo 500 nm and Mo 1000 nm compared to Mo 300 nm; with an increase in thickness, conformal coverage of Mo adatoms on a substrate also increases. Mo 300 nm has small circular grains while Mo 500 nm has uneven continuous big grains in size. Closed tight circular grains have been observed for Mo 1000 nm and this may lead to less grain boundary spacing compared to Mo 300 nm which in turn results in low resistivity of Mo 1000 nm. From the literature survey, it was found that the shape of Mo grain is deposition parameter dependent. Y. C. Lin et. al. [24] inferred that the mackerel shape of Mo grains is a result of high sputtering power which leads to densely packed structure. Subhash M. Pandharkar [26] reported that the shape of Mo grains is dependent on the source to substrate distance. With an increase of source to substrate distance, mackerel changes to circular grains, and meanwhile mackerel has less optical reflectivity compared to circular grains.

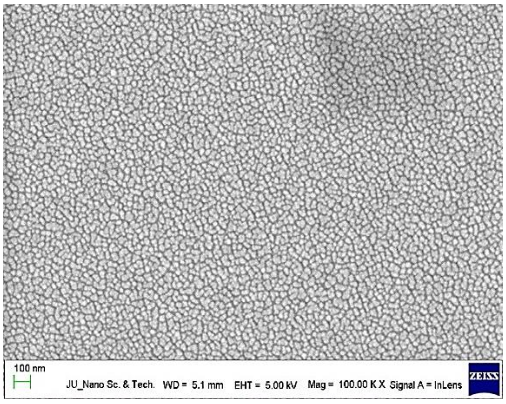

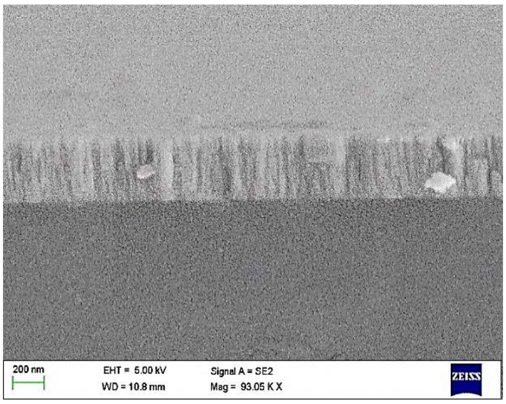

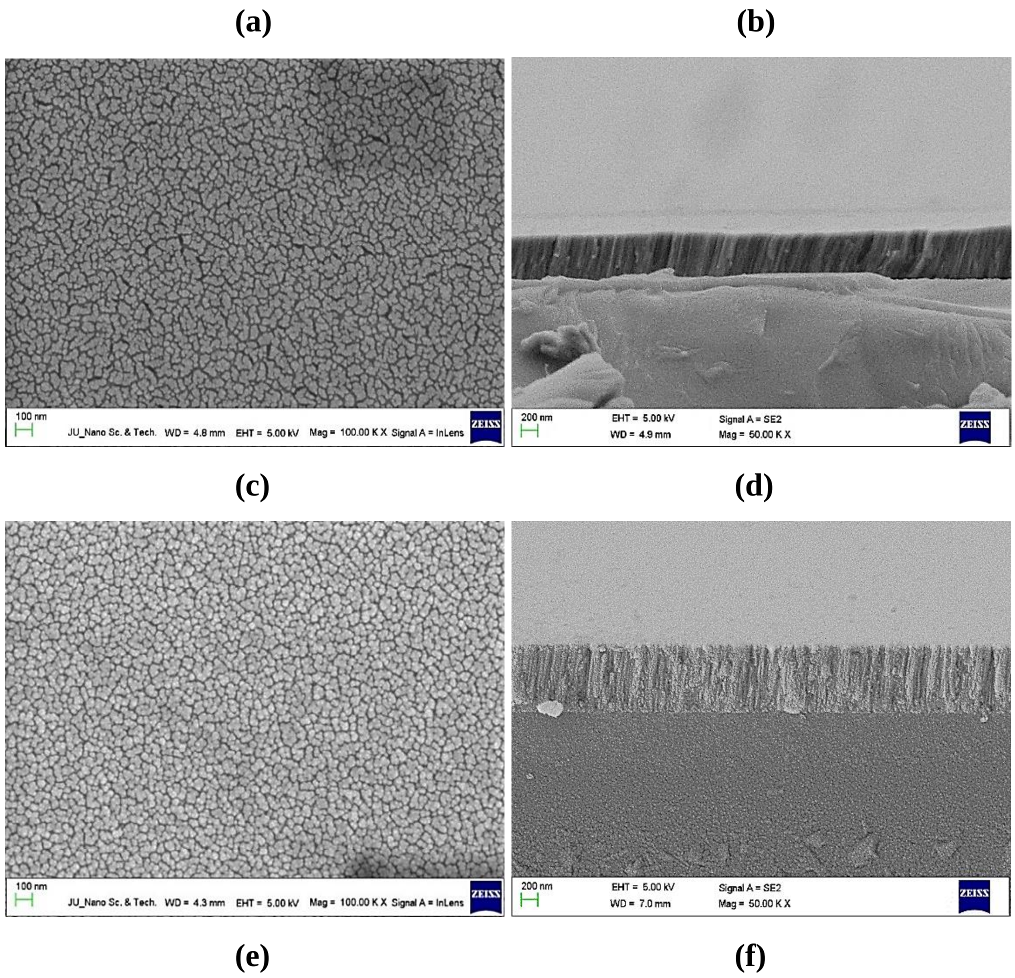

Fig. 3.11: Scanning Electron microscopy top and cross-sectional images of Mo bilayer thickness (a, b) 300 nm, (c, d) 500 nm, and (e, f) 1000 nm.

3.6 Nanosecond Laser Scribing

For structuring the multilayer CIGS thin-film solar cell module, serial monolithic interconnection provides an isolating electrical path for many solar cells in the photovoltaic module. The laser patterning process includes different steps P1, P2, and P3 at different stages of module manufacturing. To develop a highly efficient solar module, the photovoltaic cell should be segmented with low series resistance and high shunt resistance to generate high open-circuit voltage [27]. An artwork of laser patterning provides high precision, high speed, narrow scribe width, less heat affect zone, reconfigurable electric isolation which is a prerequisite and desirable for a highly efficient CIGS solar cell module. Laser scribing has excellent merits over mechanical scribing because it is non-contact, less mechanical stress, reduces the cost of ‘tip’, and less processing time. Laser scribing is a selective removal or also known as ‘selective ablation’ of the metallic thin layer above the substrate. The different types of laser interact with a variety of materials for their enormous application has been investigated.

The selective ablation process of thin films using different laser systems involves as many as possible thermo-physical and optical parameters. For different laser depend on the time scale, process such as the photochemical process for longer laser pulse more than 1 ns, thermodynamical process such as (thermal diffusion, fusion, and/or explosion) for more than 10 ps, the transformation of energy from electron to lattice for more than 1 ps, thermalization of electrons, avalanche ionization and photo-ionization process takes place for laser pulses more than 100 fs, 50 fs and 1 ps respectively occurs [28]. Generally, the ablation process is governed by material melting followed by the evaporation process. Electron-photon interaction occurs when laser with energy E’ induces in material, further due to electron-lattice energy exchanges, kinetic energy elevates which gives rise in temperature of the material. In the nanosecond laser regime, irradiation of pulse energy in material leads to heating of the material, and then energy spreads by heat conduction. Phenomenon such as melting or evaporation in material occurs. Laser pulse duration has effects on threshold fluence and effective thermal penetration depth (I_{eff}) [29, 30]. The effect of the laser pulse to a depth at which heat transports are known as effective thermal penetration depth. For the laser ablation process, both thermal diffusion length (I_{th}) and optical penetration depth (I_{opt}) play an important role. The mathematical expression for effective thermal penetration depth is described in equation (3.2).

$$I_{eff} = I_{opt} + I_{th} \tag{3.2}$$

For metals, laser source acts as a surface heat source because $I_{opt} << I_{th}$ and metals are strong absorbing material. According to equation 3.3, a short pulse regime i. e. nanosecond pulse ablation is directly dependent on applied pulse length shown in equation (3.3):

$$I_{eff} = \sqrt{2\chi\tau_p} \tag{3.3}$$

where χ and τ_p are thermal diffusivity of material and applied pulse length, Ablation threshold fluence is assumed to be a photothermal-dependent process.

The thermodynamic model is used to describe the ablation threshold fluence depend on film thickness and optical property. Irradiation of laser pulse energy induces a temperature rise in the volume needed for melting, which is defined by equation (3.4);

$$\Delta T_m = \Delta Q / C_l \tag{3.4}$$

where T_m is melting temperature, Q is absorbed laser energy, C_l is the heat capacity of the lattice. A simplified model mentioned in equation 3.5 determining the amount of ablation threshold fluence is obtained based on the above equation is described below.

$$F_{th} = \frac{\Delta T_m}{(1-e^{-\alpha d})(1-R)} \left[\rho_f c_f - \left(\frac{I_{th,s}}{I_{th,f}}\right)\rho_s c_s\right] L_f + \frac{\Delta T_m}{(1-e^{-\alpha d})(1-R)} l_{th,s} \rho_s c_s \tag{3.5}$$

and denote film and substrate quantities, is ablation threshold fluence, α is optical absorption coefficient, d is the thickness of the film, ρ is the density of mass, R is optical reflectivity of film, is the minimum dimension of heated volume. Three different types of ablation threshold fluence comportment have been observed using the above equation (3.5)

$$\begin{cases} \text{more } E_p \text{ for } d \ll I_{opt} \ll I_{eff} \text{ and } L_f = d, \left(1 - e^{-\alpha d}\right) \sim 0 \text{ when } d \sim 0; \\ = \text{'d' as } E_p \text{ totally absorbed for } I_{opt} \ll d \ll I_{eff} \text{ and } L_f = d, \left(1 - e^{-\alpha d}\right) \sim 1; \\ \text{no more 'd' dependent as } E_p \text{ totally absorbed for } I_{opt} \ll I_{eff} \ll d \\ \text{and } L_f = d, \left(1 - e^{-\alpha d}\right) \sim 1; \end{cases}$$

Laser interacting with material induces a shockwave due to plasma near the front surface. A shockwave propagates in layer and pressure is developed inside it [31, 32]. Shockwave thermally conducts the cooler layer inside the film; the layer gets heat up and the material's liquid phase ousts out due to pressure recoils from the rear to the front surface. Compressive waves evolved and propagated through film and reach the rear surface of the film. After reaching the rear surface, compressive waves release back in the same direction and another wave gets reflected from the rear surface. Continuous refraction waves were developed and when two refraction waves coincide, the tensile stress level is high. Finally, the layer gets 'ablate' or 'spall' from the substrate surface. Though laser pulse decay according to Beer Lambert's law, the rate of ablation at the surface drops down and shock wave gets attenuate due to continuous concatenating propagation of refraction waves in film. Thus, it was observed that shockwaves become triangular [33]. On imposing laser on Mo thin film, amazingly we could be able to notify a triangular shock wave impression on the surface of Mo thin film shown in Fig. 3.12.

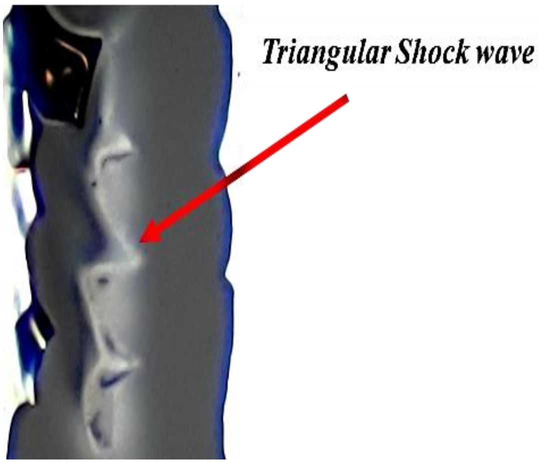

Fig 3.12: Triangular shockwave due to laser beam interaction with the Mo layer.

Geometrical locus of laser irradiated spot area will help to determine the ablated area per pulse according to equation (3.6) mentioned below:

$$A^{*} = \pi R^{2} - 2\left(R^{2}\arccos\left(\frac{\Delta Y}{2R}\right) - \frac{\Delta Y}{2}\sqrt{R^{2} - \frac{\Delta Y^{2}}{4}}\right) \quad (3.6)$$

Distance between two consecutive laser pulse spot centers shown in Fig. 3.13 can be calculated with the help of equation 3.7, where the speed of scribing (v), the radius of the spot (R), and pulse repetition rate (f).

$$\Delta Y = v * \frac{1}{f} \quad (3.7)$$

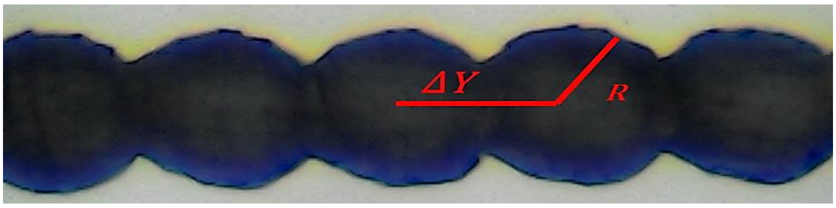

Fig: 3.13: Representation of distance between two consecutive laser pulse spots at center.

In our experiment, we used a Nanosecond Pulsed Fiber Laser Scribing System (make: Sahajanand Laser Technology, Gujarat, India) source as Nd: YAG (IPG Photonics Germany). The optical characteristics of our laser are described in Table (3.6).

Table 3.6: Operating Optical Characteristic of Nd: YAG Pulsed Fiber Laser.

Characteristics of Nd: YAG Pulsed Fiber Laser (IPG Photonics)	**Output**
Nominal Average Output Power	50 W
Peak Power	~ 8.33 kW
Central Emission Wavelength	1064 nm
Output Power Adjustment Range	10 - 100 %
Pulse Duration	120 ns at 50 kHz
Pulse Energy	1 mJ at 50 kHz
Pulse Repetition Rate	500 kHz
Beam Quality (M^2)	2.0
Output Beam Diameter ($1/e^2$)	7.5 mm
Scanning Table Speed (X-Y Movement)	150 mm/s
Galvo Scan speed	10,000 mm/s

Two different optics have been installed in our laser system. First, we experimented using the YAG Focusing lens having focal length 77 mm and multilayer antireflection coating of high damage narrow band 1064 nm. The input beam to the focusing lens is 7.5 mm in diameter and the spot size on the flat field is around 36 μm. Second, we used the F-theta lens of 100 mm focal length with two Galvo mirrors (X and Y) for fast laser beam steering. The input aperture was 10.0 mm, and the maximum scan angle was ±15 ° with a resolution of 12 μrad. F-theta lens has advantages over Focusing lenses such as fast scanning, precession in marking, cutting, and engraving, delivery of focused beam over multi-points on field area, less and compact optics, and light scan head [34]. Fig 3.14 and Fig 3.15 (a, b, and c) represent the laser scribing system and P1 laser scribing process of the Mo layer on a glass substrate. The above figures describe how a laser interacts with a thin-film surface, penetrates through it, and finally removal of thin-film layer. Fig. 3.16 (a) is an image of Mo thin film before laser irradiation on its surface. Laser pulse spreads heat energy on the surface of Mo thin film. Due to this pressure is developed which creates stress in the film above its fracture limit and cracks are formed in the regular pattern observed in Fig. 3.16 (b). Along with a kerf width temperature distribution

Fig 3.14: Laser Scribing unit.

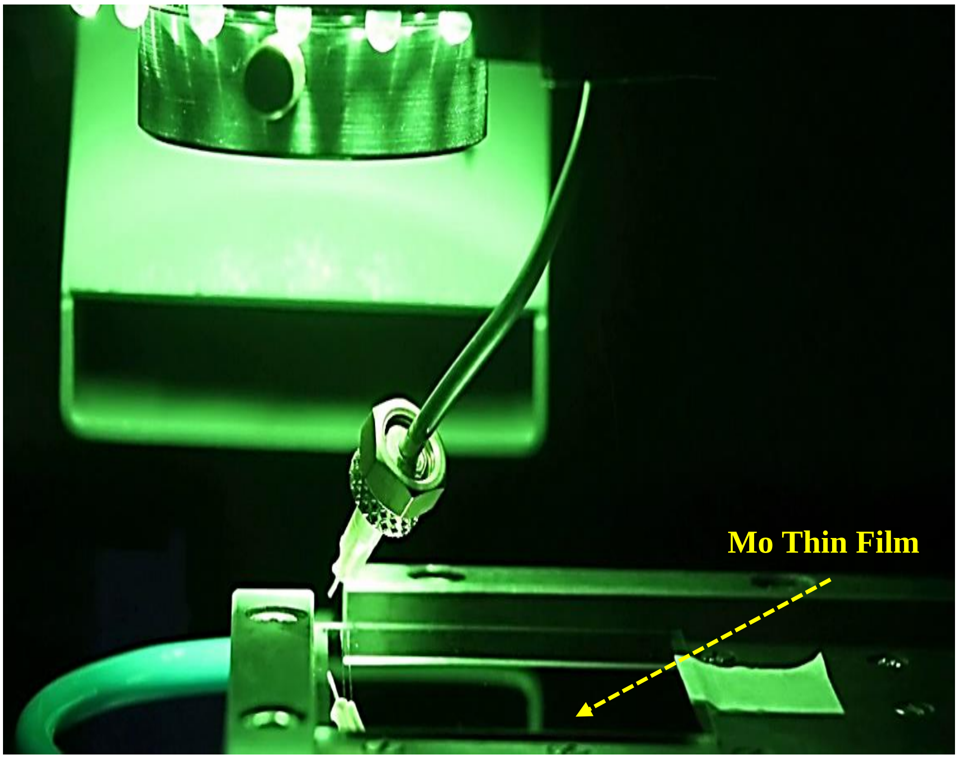

(a)

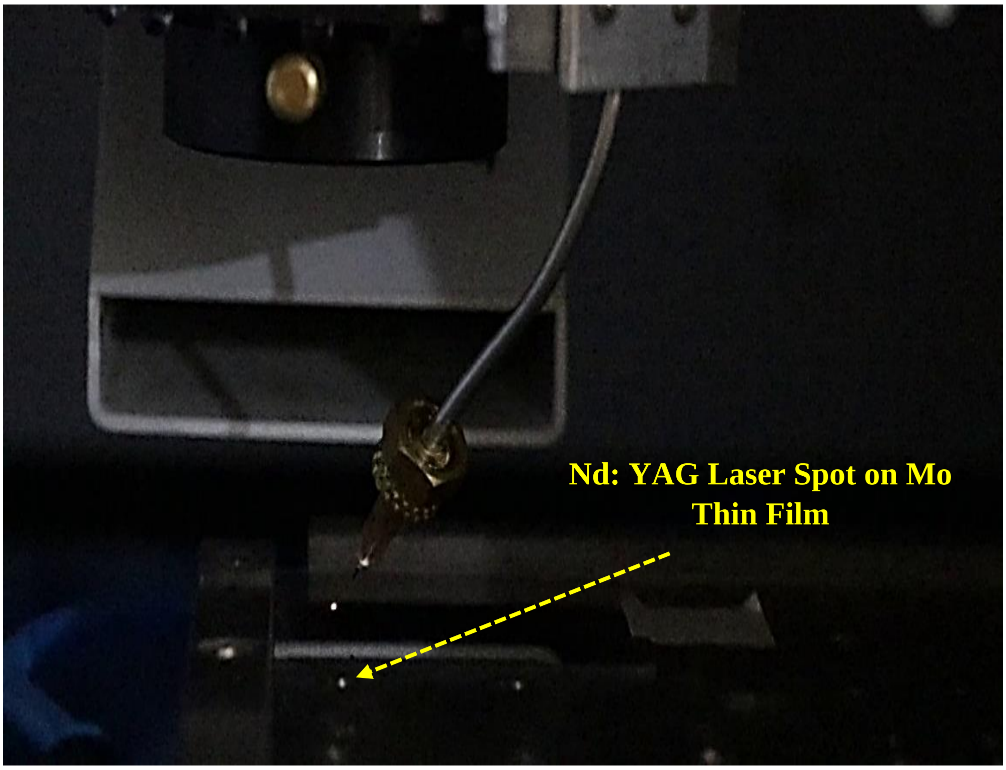

(b)

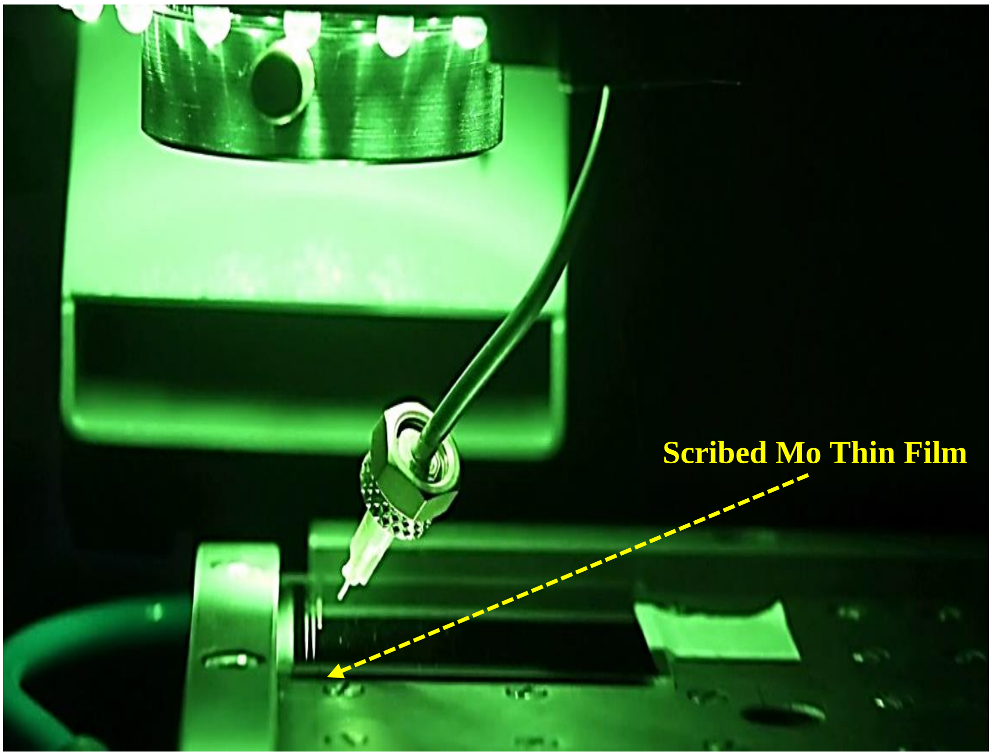

(c)

Fig 3.15: Laser scribing process steps

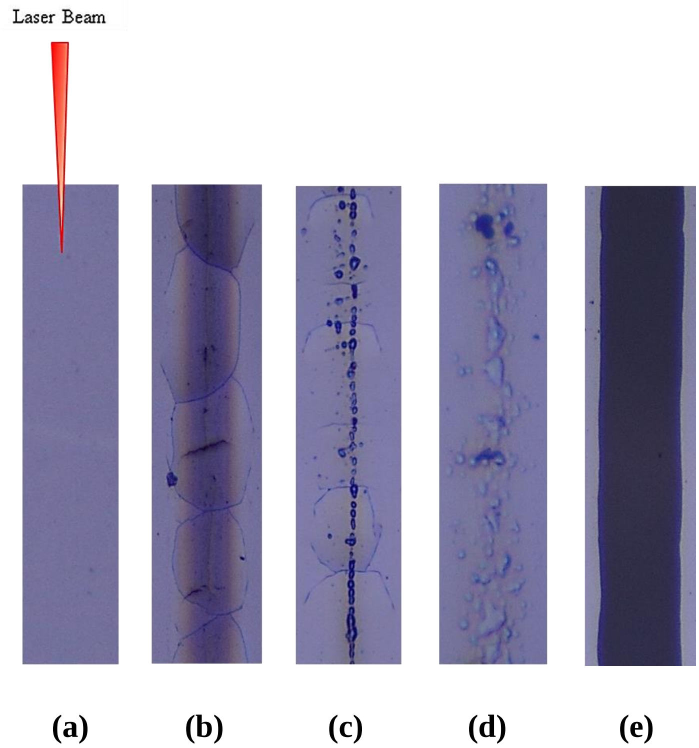

Fig 3.16: (a) Mo thin Film, (b) Heat distribution at the surface, (c) train of pulse, melting Mo surface, (d) evolution of layer from inside layer, and (e) complete removal of Mo layer.

profile adopts a gaussian shape. To ablate the layer more pulse energy is required to melt the surface and inside the layer. In Fig. 3.16 (c), enough amount of pulse energy is available to melt the surface, and further this pulse energy propagates inside the layer. Accumulation of small heat volume inside the layer creates recoil pressure, melting of material takes place. Mo layer protrudes from the rear surface and forms a bulgy shape at the front surface as shown in Fig. 3.16 (d). Finally, the clean and complete ablation of the Mo layer occurs as shown in Fig. 3.16 (e). Laser parameters such as pulse energy, pulse repetition rate, scribe scan speed, pass delay, Z-focus have been optimized for a P1 scribing process.

3.6.1 YAG Focusing Lens

3.6.1.1 Pulse Repetition Rate

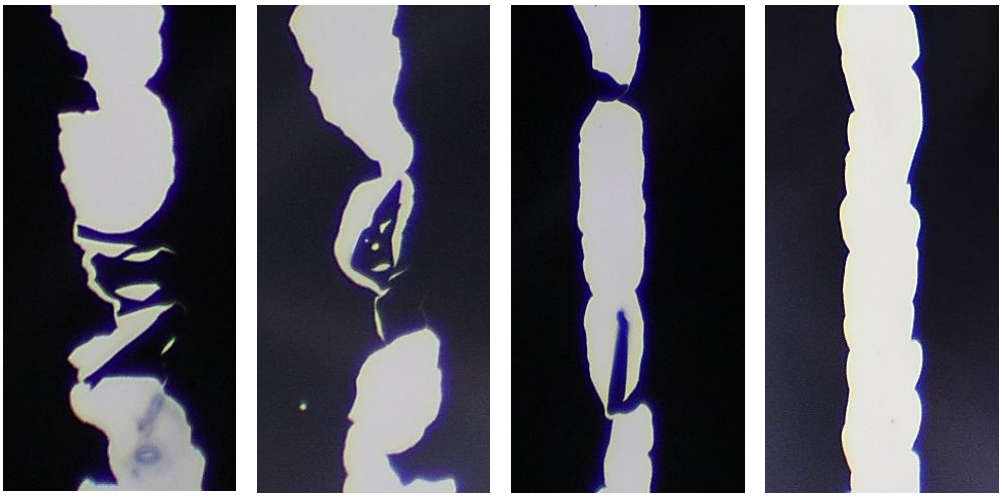

(a) (b) (c) (d)

Fig 3.17: P1 laser scribing at 150 mm/s, 2 pass, 1.9 W, 10 sec pass delay, 39.1 mm-Z focus and pulse repetition rate (a) 10, (b) 25, (c) 100 and (d) 450 kHz.

The relationship between the train of laser pulses and pulse-to-pulse overlap affects the ablation process. The laser has a Gaussian temporal profile. The nanosecond laser possesses the melt dynamics in which the melt ablation process is governed by temperature distribution profile and heat diffusion length [35]. Pulse Repetition Rate (PRR) was varied from 10 to 450 kHz with laser power 1.9 W and scribing speed 150 mm/s. Fig. 3.17 (a) shows the microscopic images of laser ablation bilayer Mo thin film 1 µm thick. At lower PRR i. e. at 10 kHz, the train of laser pulse possesses high pulse energy and meanwhile, pulse duration also increases. Due to high pulse energy 190 µJ and pulse duration, the penetration depth of absorbed laser irradiation increases. The shock wave propagates along the pathway to distribute the thermal energy along the sideways of the scribe regime. The width of the measured scribe was 210 µm. Due to which there is a wide ablation area of the Mo layer with uneven edges. The measured pulse-to-pulse overlap is only 50 %. Laser scribing speed was 150 mm/s, some of the laser pulses could not be able to interact at the surface of the Mo layer. This hinders the continuous scribe isolation of Mo thin film. Due to high pulse energy, there is thermal damage to film and form circular spot deep down in the Mo layer or Glass\Mo interface. There is a possibility of surface damage to the glass. Further, the experiment proceeds by increasing

PRR. The scribe width slightly decreases to 180 μm shown in Fig. 3.17 (b). Pulse-to-pulse overlap increase to 80 %, but still complete isolation of Mo film was not achieved. It seems there is a mismatch of laser scribing process parameters viz. PRR and speed. The threshold fluence decreased to 0.3 J/cm^2. On increasing PRR to 100 kHz, repetitive sequential circular fine edge ablation was observed as shown in Fig. 3.17 (c). The pulse duration and pulse energy decrease due to an increase in PRR. Pulse overlap hike to 95 %. Complete isolation was still an engrossing challenge because partially Mo thin film was cleanly ablated; bridges were still present to create a shunt path which deteriorates the performance of the CIGS solar cell module. Finally, PRR increased to 450 kHz, and pulse to pulse overlap increased to 98.8 %. As such there is no drastic change in pulse-to-pulse overlap compared to 100 kHz; therefore, there is a slight increase in inscribe width 138 μm compared to 114 μm at 100 kHz. Of course, at 450 kHz PRR, there are numbers of the train of the pulse with low pulse energy 4.2 μJ. At high PRR, laser pulse has a short duration of time and less energy to interact and penetrate through the layer. This helps to reduce thermal damage at the surface of Mo thin film, the interface of Mo/SLG, and as well as the surface of glass shown in Fig. 3.17 (d). Complete and clean removal of the Mo layer was observed with ‘no heat-affected zone”. The edges are still uneven in shape but will not affect the performance of the solar cell.

3.6.1.2 Laser Scribing Speed

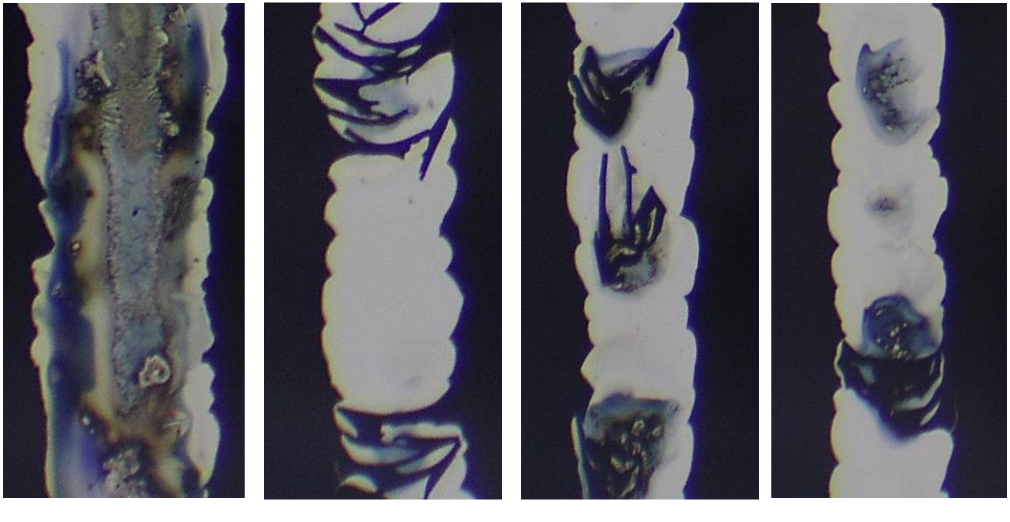

(a) (b) (c) (d)

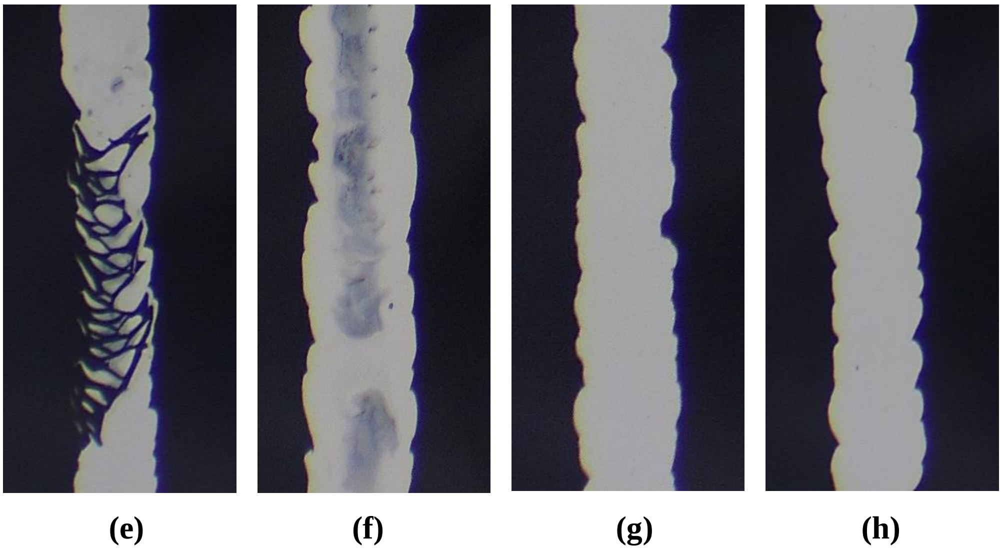
(e) (f) (g) (h)

Fig. 3.18: P1 laser scribing at 450 kHz, 2 pass, 1.9 W, 10 sec pass delay, 39.1 mm - Z focus with scribing speed (a) less than 25 (b) 25, (c) 30, (d) 35, (e) 40, (f) 50, (g) 100 and (h) 150 mm/s.

For high throughput and fast industrial processes, the speed of the scribing process adds new interesting facts for clean electric isolation of Mo thin film [36]. Our laser has the capability of achieving x-y scanning table speed to 150 mm/s. To evaluate the correlation between laser scribe speed and the quality of scribe, laser scribe was varied up to 150 mm/s as shown in Fig. 3.18. Below 25 mm/s speed, there is an eruption of molten Mo layer in the regime and further high protruding leads to bad, unclean isolation of layer. It was observed that due to low scribe speed, the pulse energy was able to thermally melt the layer by heating due to which swiftly stress is developed, leading to phase transition in the Mo layer shown in Fig. 3.18 (a). This creates a broad scribe width of 168 μm. As PRR is high 450 kHz with high pulse-to-pulse overlap and low scribe speed and increases in fluence energy results in the resilient of Mo layer with structure deformation. Partial removal of the Mo layer as shown in Fig. 3.18 (b) was observed at 25 mm/s laser scribe. The measured scribe width was 138 μm. No melts or re-solidification of layer appeared but still, 25 mm/s scribe speed fails for complete removal of Mo layer. An increment in laser scribe speed from 30 mm/s to 40 mm/s abruptly broadens the scribe width. Along with partial removal and irregular edge pattern, the heat-affected zone shown in Fig. 3.18 (c-e) in the center was observed. The laser fluence creates a large heat volume per pulse where the solid-liquid phase transition takes place which further damages the surface of the substrate. At 50 mm/s the laser shock wave is failed to direct the solid-vapor transition phase. Still, a small volume of heat was trapped beneath the Mo layer shown in Fig. 3.18 (f). 100 mm/s laser speed astonished us for clean kerf with moderate change in scribe width. However, kerf edges shown in Fig. 3.18 (g) were still wavering along the scribe length. No cracks melt, bridges, burs, heat affected zone found here. Finally, at 150 mm/s laser fluence was competent to detach the Mo layer from the glass substrate surface with acceptable edges shown in Fig. 3.18 (h). The scribe width was slightly increased to 156 μm. The pulse-to-pulse overlap is imperceptible with variable laser scribe speed at constant pulse repetition frequency.

3.6.1.3 Different Laser Pass Delay

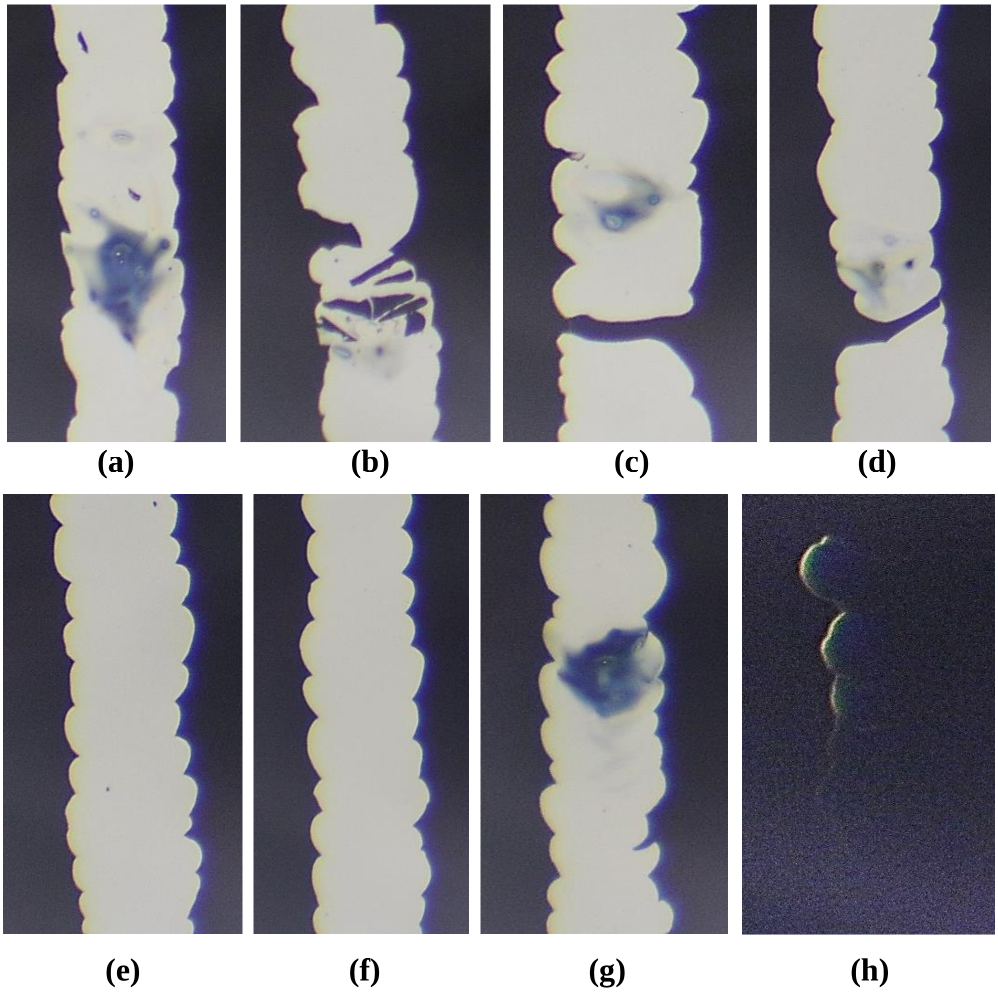

Fig. 3.19: P1 laser scribing at 450 kHz, 150 mm/s speed, 2 pass, 1.9 W, 39.1 mm-Z focus and pass delay (a) 0.1, (b) 1, (c) 2 (d) 5, (e) 10, (f) 15, (g) 20 and (h) 25 seconds.

A single-pulse shot was not enough for complete removal of the Mo layer, therefore double shots of the laser were imposed on the Mo layer. The duration between two shots influences clean isolation [37]. Choosing an appropriate time delay between two laser shots is quite reasonable for clean isolation. Effect of pass delay on clean removal of Mo layer at constant scribe speed 150 mm/s and PRR 450 kHz is shown in Fig. 3.19. If the pass delay is very small, then the layer has more thermal energy absorbed in it. Excessive energy above the heat of vaporization, damage the layer by phase transition or recast the layer. For a 0.1 second pass delay shown in Fig. 3.19 (a), thermal damage of the Mo layer was observed. In the range of 1-2-5 seconds pass delay channels, bridges, and spots due to thermal damage were seen. Insufficient thermal energy distribution along the Mo layer leads to incomplete removal of the Mo layer shown in Fig. 3.19 (b-d). Delay of 10 seconds to 15 seconds shown a clean removal of Mo layer without any channels or bridges shown in Fig. 3.19 (e) and (f). Initially, the laser pulse distributes enough thermal energy to melt the layer, and the second laser pulse rises temperature to the heat of vaporization of Mo material before Mo gets cooled after the first laser shot. It was found that on increasing pass delay to 20 sec to 25 sec, clean removal of the Mo layer process was hindered. On absorbing laser pulse shot, a shockwave propagates through-thickness of the Mo layer where the temperature inside layer may rise to some extent but not up to the melting point of the Mo layer. After complete decay of the laser pulse shot, the Mo layer gets cooled. As there is no thermal energy store in the Mo layer, there is no phase change. Even on absorbing the second laser pulse shot, the temperature of the Mo layer could not rise to the heat of vaporization, but a still small volume of heat energy is trapped inside the layer. A partial change in phase was observed shown in Fig. 3.19 (g) and (h).

3.6.1.4 Different Laser Power

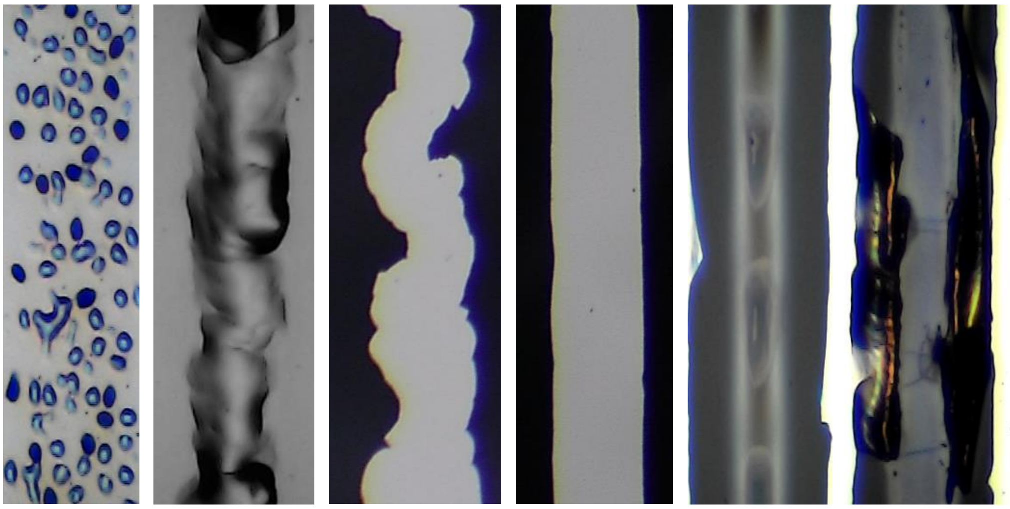

(a) (b) (c) (d) (e) (f)

Fig. 3.20: P1 laser scribing at 450 kHz, 150 mm/s speed, 2 pass, 39.1 mm - Z focus, pass delay 10 sec and power (a) 0.65 W, (b)1.08 W, (c) 1.4 W, (d) 1.9 W, (e) 2.45 W and (f) 2.85 W.

Laser power is a primary important factor for the clean and narrow scribe. Choosing competent pulse energy will enhance the processing ability of the scribing process. If pulse energy is too low, the layer will be deprived of the pulse energy of the thermophysical phase transition resulting in unscribe or partial change in a phase transition [38]. On the other hand, if the pulse energy is too high, then to reduce and dump excess heat, the layer and substrate may get deeper damage. To avoid such issues, one can select the appropriate pulse energy for a clean and burr-free, and less heat-affected zone scribing process. For the P1 process on bilayer Mo thin film, we investigated the minimum required pulse energy for complete clean ablation of Mo bilayer shown in Fig. 3.20. For power, less than 0.65 W, laser pulse energy failed to reach the melting temperature of the entire layer. Slightly, surface melting was observed shown in Fig. 3.20 (a). This confirms that still more pulse energy is required to reach the threshold Mo bilayer. On increasing laser power to 1.08 W, we found a phase transition. Mo plume was observable over the entire scribe region shown in Fig. 3.20 (b). Here the pulse energy was increased to 2.4 μJ. But only the melting of Mo bilayer was adjudged. For the ablation threshold more energy i. e. about 1.4 W was enough. In Fig. 3.20 (c), the Mo bilayer gets ablated, but the edges were not sharp and clean. This indicates the need for slightly more pulse energy than 2.4 µJ. The measured scribe width was 80 µm. Subsequently, on imposing laser beam with 1.9 W power, impulsively complete clean burr-free center irradiated area and edges were marked. 4.2 µJ pulse energy efficiently ablates the entire layer. Due to an increase in pulse energy, the scribe width increases to 154 µm. Both bilayer Mo and glass interface got mutilate with pulse energy 5.4 µJ. The deep oval-shaped crater at Glass/Mo interface formed at 2.45 W laser power shown in Fig. 3.20 (d). Bilayer Mo completely got ablated but another scribe regime at the center region with crater was visible. This depicts that at 2.45 W power, damage at Mo/SLG interface begins. Further on increasing laser power to 2.85 W not only bilayer Mo but glass surface also got damage. 6.3 µJ pulse energy erodes Mo layer; debris and maybe even glass and redeposits it. The edges are more damaged as well as width increase to 213 µm shown in Fig. 3.20 (e) and (f).

3.6.1.5 Depth of Focus

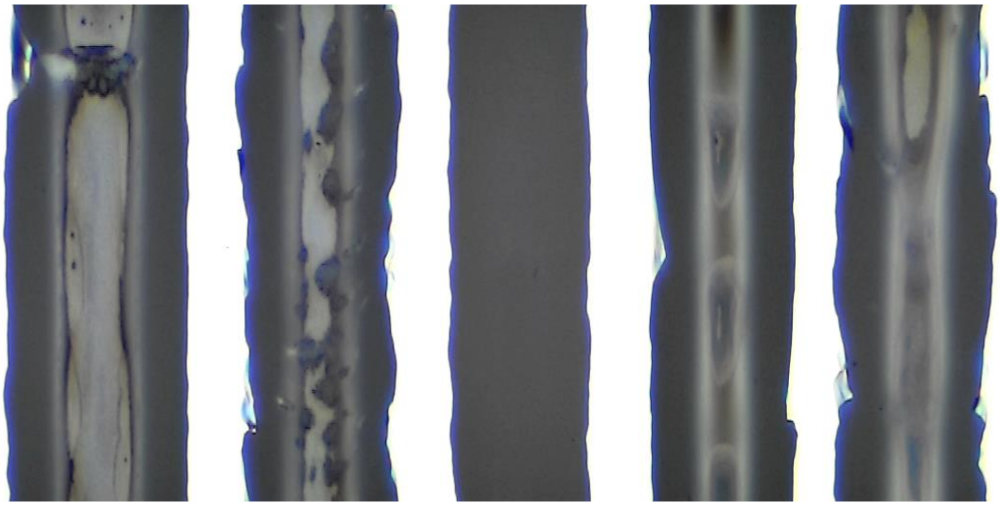
(a) (b) (c) (d) (e)

Fig. 3.21: P1 laser scribing at 450 kHz, 2 pass, 150 mm/s speed, 1.9 W power, pass delay 10 seconds and Z-Focus (a) ΔZ = 37.1 mm, (b) ΔZ= 38.1 mm, (c) ΔZ = 39.1 mm, (d) ΔZ = 40.1 mm, and (e) ΔZ = 41.1 mm.

Beam Divergence has an additional impact on the scribing process. A focused laser beam results in a clean scribing process but as soon as defocusing starts taking place Mo layer as well as the Glass/ Mo interface and surface of the glass gets thermally damage [39]. As shown in Fig. 3.21 (c) at ΔZ = 39.1 mm clean, the burr-free scribe was observed. While at ΔZ = 38.1 mm laser beam got defocused shown in Fig. 3.21 (b) and the Mo layer start getting redeposited at the edges. Further, on defocusing to ΔZ = 37.1 mm, Mo layer form bridges/ channels shown in Fig. 3.21 (a) in addition to its glass surface also got damage. Moving towards another end as shown in Fig. 3.21 (d) where ΔZ = 40.1 mm, Mo layer scribes well but at the center regime, even Mo/SLG interface transition phase was observed. This resembles the defocusing of a laser beam. A similar effect as shown in Fig. 3.21 (e) was observed for ΔZ = 41.1 mm.

3.6.2 YAG F-Theta Lens

3.6.2.1 Laser Power

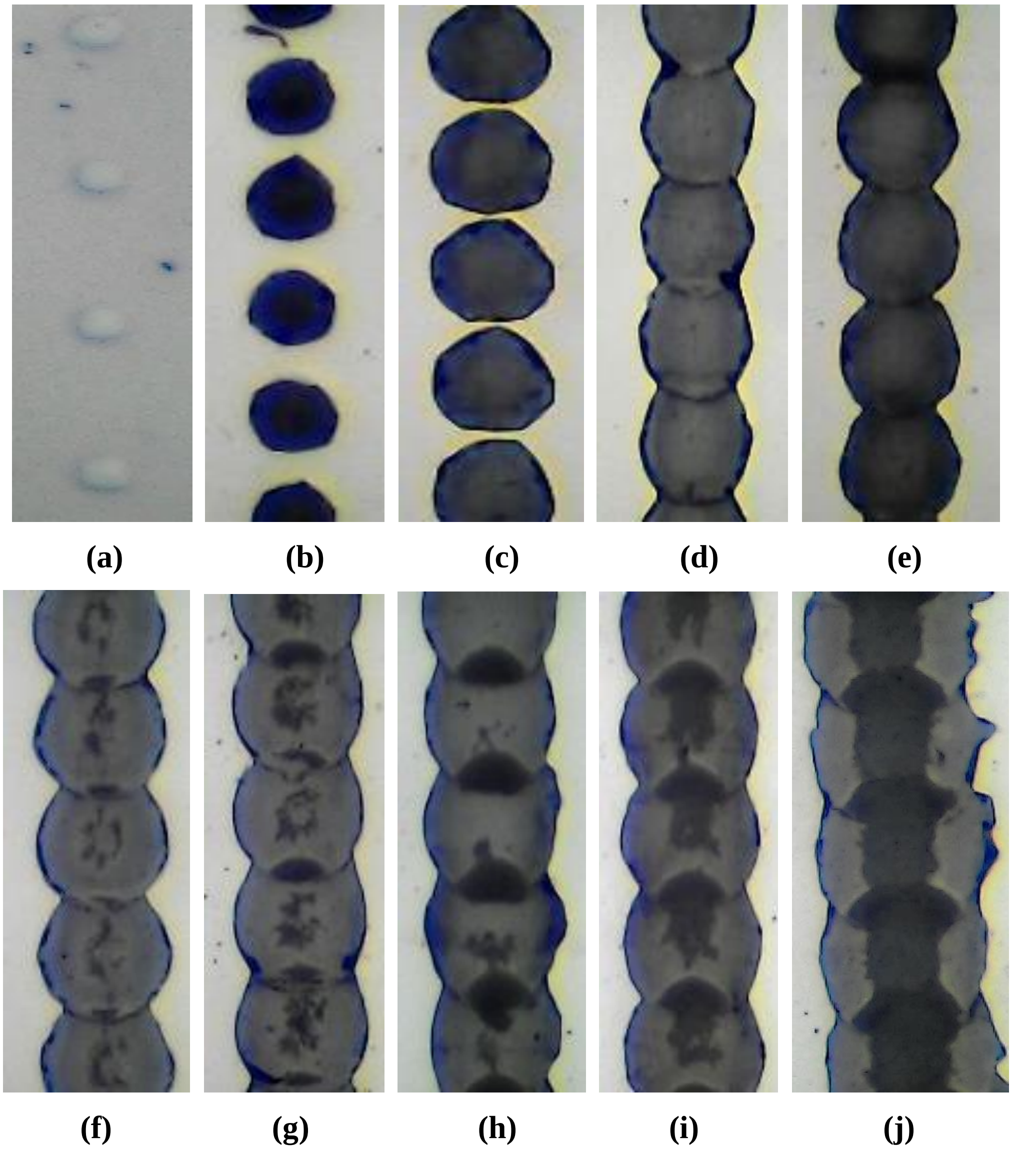

(a) **(b)** **(c)** **(d)** **(e)**

(f) **(g)** **(h)** **(i)** **(j)**

Fig 3. 22: P1 laser scribing at 20 kHz, 3500 mm/s speed, power (a) 0.22 W (b) 0.65 W, (c) 1.08 W, (d) 1.4 W, (e) 1.9 W, (f) 2.45 W, (g) 3.41 W, (h) 4.45 W, (i) 5.46 W, and (j) 5.58 W.

The foremost parameter to investigate the P1 process is to manage laser fluence on Mo thin film to ablate it rather than heating [40]. We initiated with laser power 0.22 W. We found only phase transition due to low pulse energy 11 µJ. The impression of laser spot forming bulgy structure and was clearly visible, but there was not enough energy for deep penetration into layers shown in Fig. 3.22 (a). At 0.4 W, bilayer Mo thin film was discretely mottled with a laser beam at a distance apart from each other shown in Fig. 3.22 (b). Clean but interrupted ablated spot reveals that minimum pulse energy of more than 20 µJ available for complete scribe isolation. The scribe width was 48 µm. The separation between two ablated spots starts decreasing while ablated spot size increased to 54 µm when laser power 0.65 W imposed on Mo thin film. 32 µJ pulse energy dispenses slightly more heat energy due to which separation between two ablated spot decrease shown in Fig. 3.22 (c). Still, there is no continuous clean scribe. Ablated spots start overlapping each other when laser power was 1.08 W shown in Fig. 3.22 (d). Slight redeposition of melted Mo appeared at the side edges and even at the overlapping regime with 54 µJ pulse energy have a scribe line width of about 60 µm. Laser power 1.4 W dispense adequate heat energy for the complete, clean, and continuous scribe. No debris, burr, redeposition, and heat-affected zone was observed shown in Fig. 3.22 (e). Galvo with an F-theta lens and enough pulse energy 70 µJ provide precise and repeatable control over the scribing process. This results in an immaculate scribe width of 60 µm. Slight damaging started at the center and edges when laser power increased to 1.9 W shown in Fig. 3.22 (f) and further it continued increasing laser power to 5.58 W. Not only edges but overlapping regimes get badly damaged due to excessive dosage of pulse energy approximately 275 µJ pulse energy. This widens the scribe line width up to 72 µm shown in Fig. 3.22 (g-j). The Mo/SLG interface has trapped a large volume of heat energy which melts both Mo layers in addition to its glass surface too. This generates a non-homogenous phase and on cooling, this redeposited phase creates a shunt path.

Detrimental effects were noticeable with an increase in pulse energy starting from disfiguring circular scribe lines from the center towards edges with flakes.

3.6.2.2 Pulse Repetition Rate

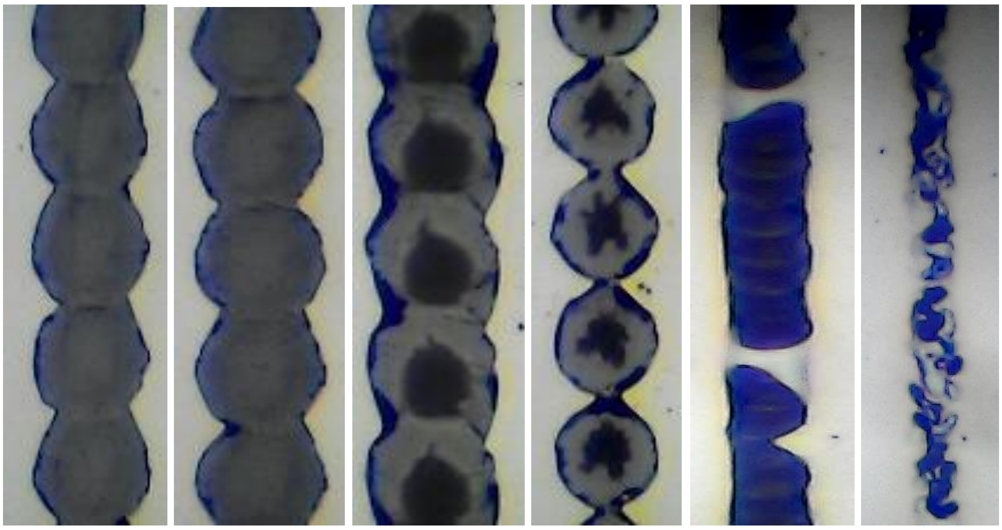

(a) (b) (c) (d) (e) (f)

Fig 3. 23: P1 laser scribing at power 1.4 W, 3500 mm/s speed, pulse repetition rate 20 kHz, (b) 40 kHz, (c) 50 kHz, (d) 100 kHz, (e) 250 kHz and (f) 450 kHz.

During the investigation for the clean scribe process, pulse repetition rate (PRR) is the second most subsequent parameter. Shown in Fig. 3.23 (a) and (b) at 20 kHz and 40 kHz, a clean and continuous scribe line with no micro-cracks and shunts and the heat-affected zone was observed. No change in scribe quality and width was observed when PRR was increased to 40 kHz. Pulse energy reduced from 70 µJ to 35 µJ, but it was enough for ablation. Compared to 20 kHz PRR fluence 2.04 J/cm^2, at 40 kHz fluence reduce to its half value i. e. 1.02 J/cm^2; no significant melt or debris was observed. Further increase in PRR, the pulse energy is more concentrated at the center regime. The laser beam distributes its energy in the Gaussian path and at high PRR i. e., 50 kHz and 100 kHz energy distribution at sidewalls are less. This has been confirmed from Fig. 3.23 (c) and Fig. 3.23 (d). Melted has been re-deposited at the side walls. The fluence has been decreased to 0.81 J/cm^2 and 0.49 J/cm^2 which was not enough for uniform ablation. The scribe width was 66 µm at 50 kHz, it reduces to 60 µm at 100 kHz. The shape of the sequential circular scribe pattern was transformed into a straight line. With a huge number and overlapping of the train of pulses at 3500 mm/s Galvo scan speed, 5.6 µJ was not enough for complete clean isolation of the Mo layer. Both parameters i. e., 3500 mm/s speed, and 250 kHz PRR are discordant with each other for producing a clean scribe shown in Fig. 3.23 (e). Fluence 0.16 J/cm^2 partially succeeded in eroding the bilayer Mo with scribe width 24 µm. Only protrusion of Mo was observed at 450 kHz PRR shown in Fig. 3.23 (f). 0.07 J/cm^2 fluence was able to create a transition in the phase of Mo by creating melt. At such high PRR and speed, pulse energy could not be able to properly interact with the Mo layer.

3.6.2.3 Galvo-Speed

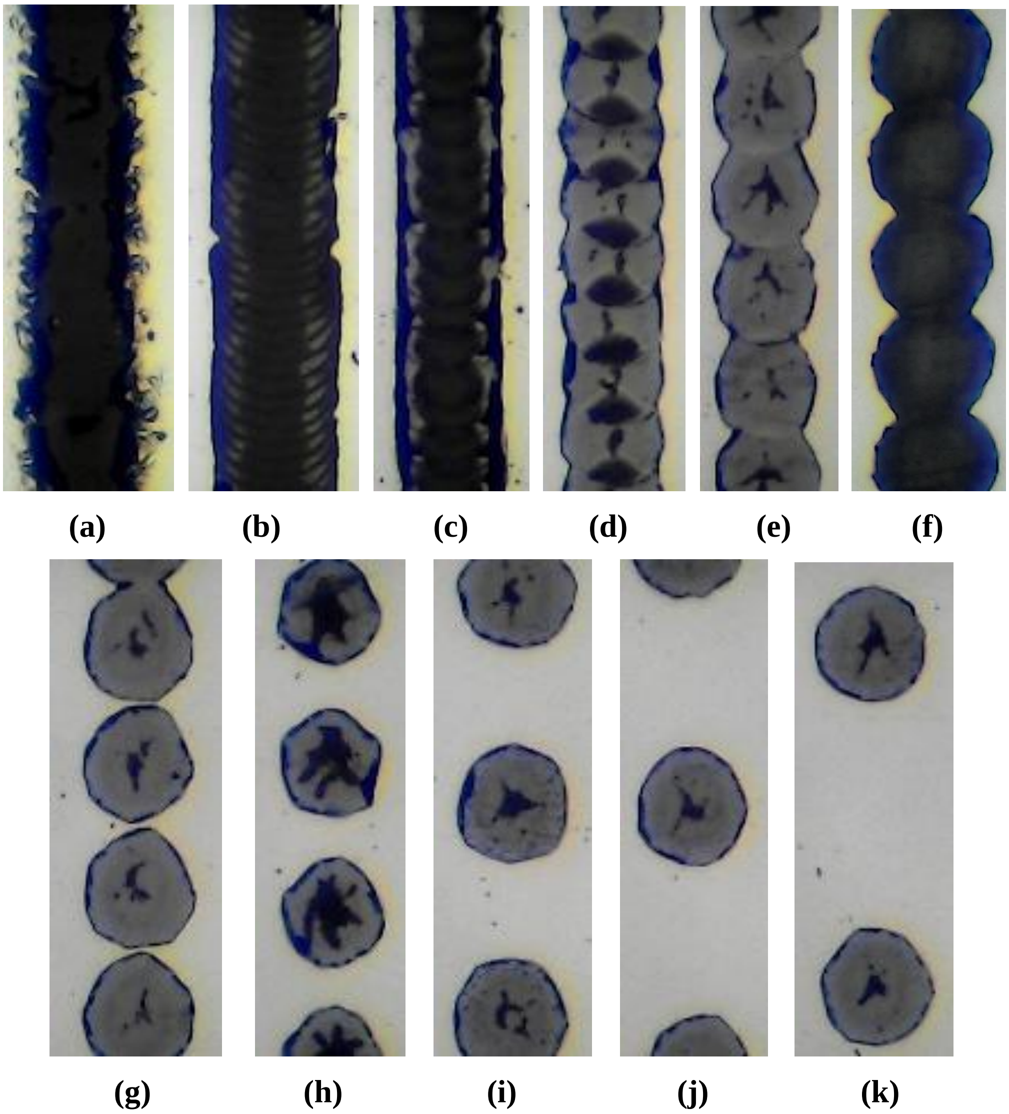

Fig 3. 24: P1 laser scribing at power 1.4 W, pulse repetition rate 20 kHz and Galvo scan speed (a) 100, (b) 500, (c) 1000, (d) 2000, (e) 3000, (f) 3500, (g) 4000, (h) 5000 (i) 7500 (j) 10,000 and (k) 20,000 mm/s.

We experimented with different Galvo assisted laser scan speed to examine the features of the Mo scribing process. Beginning with 100 mm/s, Mo melt was erupted, recasted, and stuck in the center, and flakes were spread at the edges with scribe width 48 µm shown in Fig. 3.24 (a). Due to low scan speed, high overlap, and fluence 3.87 J/cm^2 not only Mo layer melts but also soda-lime glass surface too got damage. Scribe width increase to 54 µm when fluence was 3.05 J/cm^2 at 500 mm/s. But still melt was deposited at the edges and center regime of scribe deeply thermally damaging Mo/SLG interface shown in Fig. 3.24 (b). The circular successive ablated spot was observed, but at the side walls edges, melted Mo redeposited partially creating shunt also. This behavior was observed when scan speed and fluence were 1000 mm/s and 2.47 J/cm^2 respectively shown in Fig. 3.24 (c). The shape of the scribe line started transforming at scan speed 2000 mm/s, absolutely there was a change in fluence and scribe width; but due to high scan speed, pulse energy 70 µJ damaged the overlapping region of the scribe line and partly edges too shown in Fig. 3.24 (d). This effect was reduced at 3000 mm/s scan speed shown in Fig. 3.24 (e). Still at the center slight damage was observed. A uniform, continuous clean, burr-free circular scribe line was formed at 3500 mm/s having fluence 2.05 J/cm^2 shown in Fig. 3.24 (f). Surprisingly, from 4000 mm/s to 20,000 mm/s scan speed ablated spots started separating from each other at linear increment in the distance apart. In Fig. 3.24 (g), (h), (i), (j), and (k) it is distinctly visible that ablated spot size and fluence were not affected by incremental change in scan speed. 2.47 J/cm^2 and 60 µm fluence and ablated spot size were measured. The propagation of the laser beam in vertical Z-direction is spatially prolonged depending upon the focal length of the lens and sample height [41]. We studied the quality depth of scribe by varying Z-movement of F-theta lens in the range from ΔZ= -0.8 mm to +0.8 mm. From Fig. 3.25 one it is noted that at $\Delta Z = 0$ as shown Fig. 3.25 (e) focus point, the clean scribe was obtained. As the laser beam

3.6.2.4 Depth of Focus

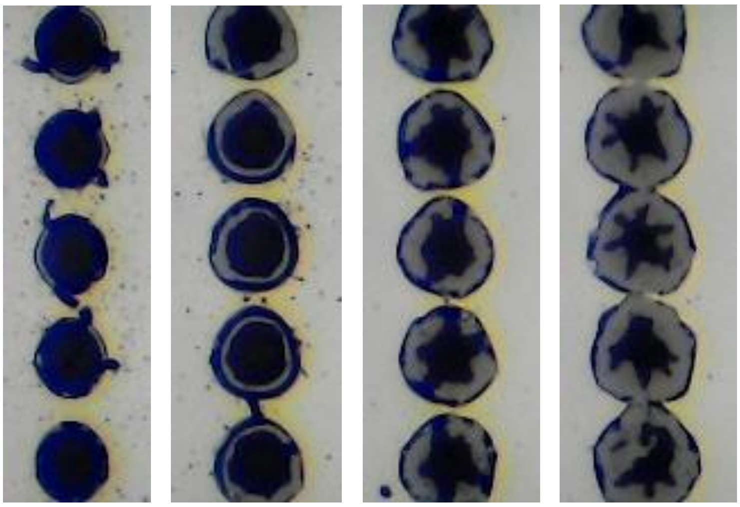

(a) ΔZ = -0.8 (b) ΔZ= -0.6 (c) ΔZ = -0.4 (d) ΔZ = -0.2

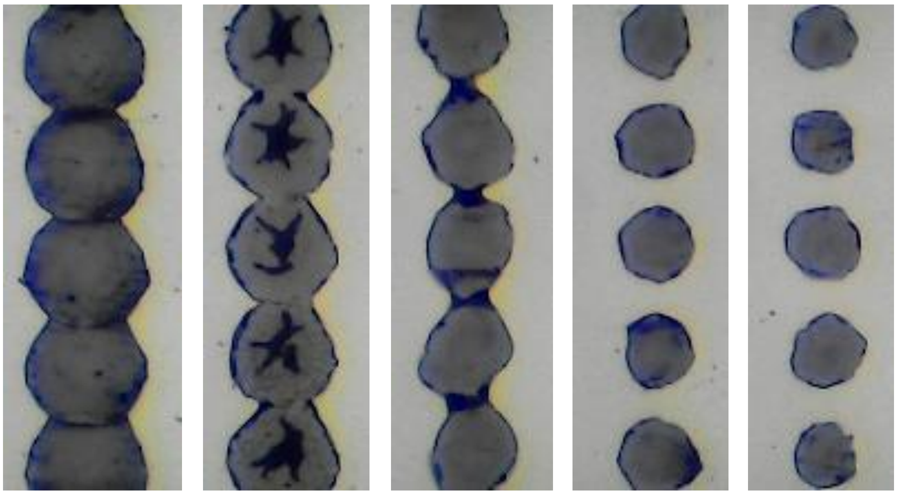

(e) ΔZ = 0 (f) ΔZ = +0.2 (g) ΔZ = +0.4 (h) ΔZ = +0.6 (i) ΔZ = +0.8

Fig 3. 25: P1 laser scribing at power 1.4 W, pulse repetition rate 20 kHz and Galvo scan speed 3500 mm/s and depth of focus ΔZ = -0.8 mm to +0.8 mm.

defocused towards Δ Z = -0.8 mm shown in Fig. 3.25 (a-d), the depth of the scribe increased. Initially, the center region of the ablated spot absorbs more pulse energy, and as defocusing reaches to ΔZ = -0.8 mm whole ablated spot has an ample amount of pulse energy which grooves deep in the glass surface too. The ablated spot size decreased from 60 µm to 42 µm shown in Fig. 3.25. Defocusing towards ΔZ = +0.8 mm as shown in Fig. 3.25 (f-i), here also initially pulse energy damage at the center but later the only separation between ablated spot increased and its size decreased. The ablation spot size decreased from 72 µm to 48 µm. These results unfold the truth that selecting an appropriate ΔZ will also be one of the key parameters for a clean, burr-free, and non-heat affected zone for the scribing process.

After thoroughly optimizing the P1 scribing parameter using YAG f-theta lens, P1 patterning was carried out on 60 x 60 mm SLG/Mo shown in Fig. 3.26 with laser power 1.4 W, 20 kHz PRR, and Galvo speed of 3500 mm/s.

Fig 3.26: Photo (using back light) of bi-layer molybdenum thin film on 60 x 60 mm square SLG using P1 scribing process with the optimized parameter of Nd:YAG fiber laser.

3.7Adhesion Test

One of the key features of the back ohmic contact for thin-film CIGS solar cells is the adhesion property of the Mo layer on the SLG substrate. For back ohmic contact adhesion between Mo and SLG should be good. Adhesion between two dissimilar surfaces is known as “Heterohesion”, while for similar surfaces “Autohesion or “Homohesion” [42]. It is manifest that factors such as type of substrate, substrate cleaning procedure, substrate temperature, rate of deposition, purity of source, source to substrate distance, pressure in the deposition chamber and glow discharge affect the adhesion between thin film and substrate [43, 44]. The adhesion test was performed based on the ASTM standard D 3359-09 (Standard Test Measuring Adhesion by Tape Test) [ASTM-D3359-09] [45]. A lattice pattern of crosshatch with 6 cuts was made in each direction of Mo thin film using Nd:YAG Laser. The prime advantage of using Nd:YAG laser was to ensure one single precise straight cut. The space between the cuts was 2 mm and 20 mm long. The pressure-sensitive tape 3M scotch tape was applied on the grid area of the Mo thin film surface. The tape was pressed by rubber squeegee to create good contact between Mo thin film and substrate. After 90 ± 30 seconds of tape application of film, remove the tape from its seizing free end without jerking. The inspection of the adhesion test was done based on the classification of adhesion test results [46]. According to many studies, it has been investigated that compression stress is good for the adhesion property of the Mo layer. At high working pressure, the tensile stress is found more in the Mo thin films that tend to adhere to the SLG substrate. Adhesion of Mo layer and SLG substrate is due to mechanical interlocking. Adhesion test was performed on bilayer Mo thin films deposited 150 W DC power. Bilayer Mo thin film passed the adhesion test. As shown in Fig. 3.27 (a), according to ASTM standard 3359-09 nine mesh have been drawn using Nd:YAG 1064 nm laser instead of using a knife, scalpel, razor blade, or any other mechanical cutting tool. The mesh has no burs, channels, melt-redeposited Mo, and heat-affected zone. The result of the adhesion test was confirmed when no peeling of the Mo layer was found. This adhesion test adds one more important fact that compare to in mechanical scribe there are major chances of peeling and damaging of layer, therefore laser scribing process is more reliable for adhesion between the Mo layer and glass substrate. Adhesion test via chemical deposition process was performed for Mo deposited at room temperature (RT) and substrate temperature (ST-215 ˚C). Both samples were immersed in 6M of NH_4OH solution. The bath temperature was 85 ˚C and the substrate was rotated in the solution for 10 minutes. Mo layer deposited at RT was peeled off during process, but Mo layer deposited at ST-215 °C withstand after the process shown in Fig. 3.27 (b). No peeling off or pinhole was observed.

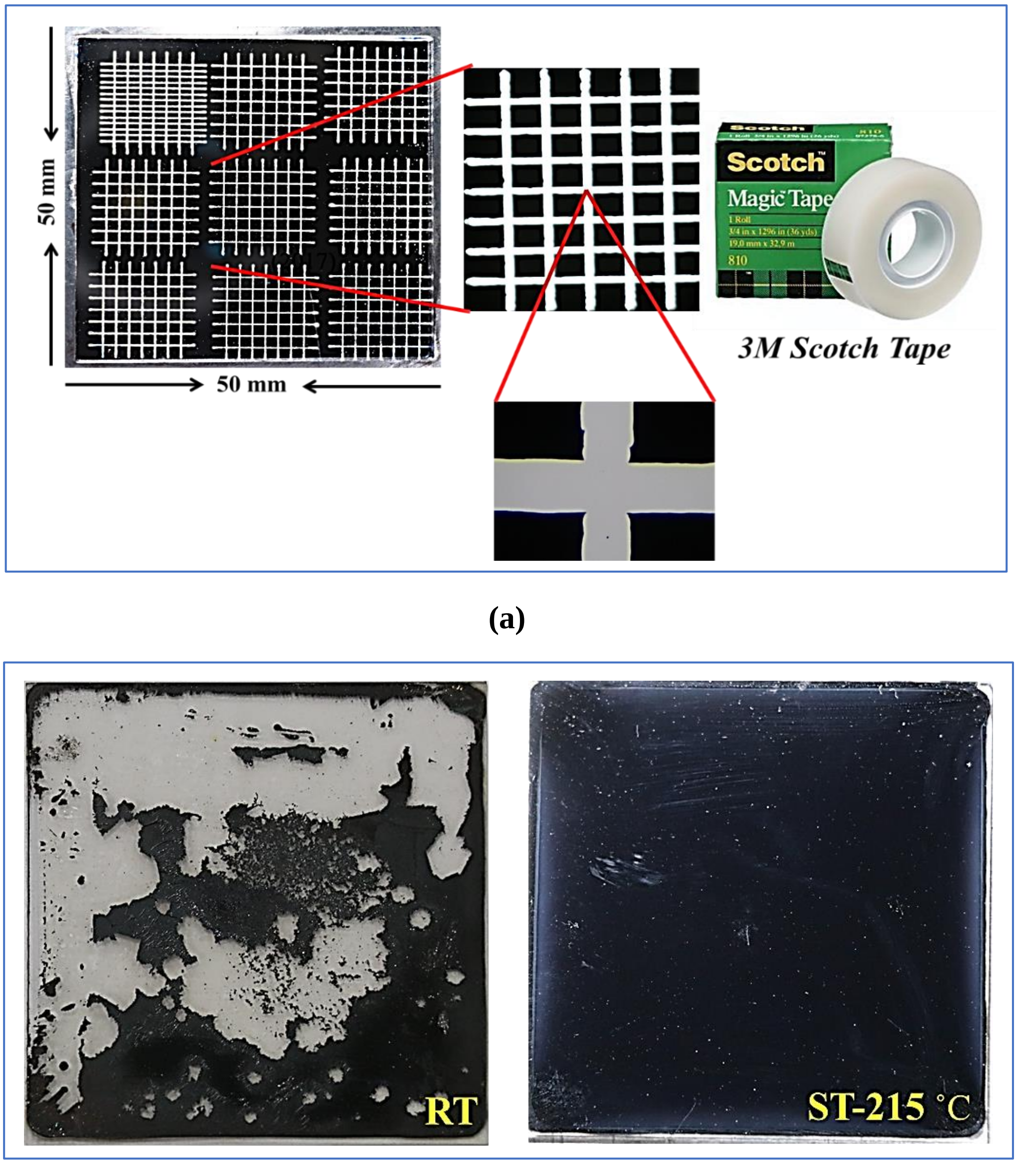

(a)

(b)

Fig 3.27: Adhesion Test of bilayer Mo thin film deposited at 150 W DC power by (a) Nd:YAG (1064 nm) Laser, and (b) 6M of NH_4OH solution.

3.8 Conclusions

In this chapter, experiments were carried out to study structural, optical, electrical, and microstructural properties of single and bilayer Mo thin film 10 mTorr and 1 mTorr deposited at (50, 100, 150, 200 W), having substrate temperature as room temperature and 215 ˚C. Mo thin film was deposited using DC sputtering technique on a soda-lime glass substrate. From the results it was concluded there is not much effect of substrate temperature upto 215 ˚C on physical and optoelectronic properties of Mo thin film compared to room temperature deposition. At 150 W, bilayer Mo thin film at room temperature has good crystallinity, 64 % optical reflectance, 0.332 **Ω**/□ sheet resistance, and dense columnar microstructure and passed adhesion test too. Minimum 500 nm is required for the Mo layer to show its capabilities as an ohmic back contact. Therefore, the above-mentioned deposition condition is favorable for depositing Mo thin film so that it can be used as an ohmic back contact for CIGS solar cell. Room temperature Mo layer fails to withstand the chemical deposition process. For monolithic interconnection, the P1 scribing process was optimized by nanosecond Nd:YAG 1064 nm laser. Laser tunable parameters such as laser power, pulse repetition rate, scan speed (X-Y movement and Galvo), pass delay, and depth of focus were examined for the P1 scribing process. For high throughput, clean, burr-free, and less heat affected zone with small scribe width was obtained using F-theta lens assisted with Galvo mirrors.

References

[1] Weimin Li, Xia Yan, Armin G. Aberle, and Selvaraj Venkataraj, *8th International Conference on Materials for Advanced Technologies, Procedia Engineering*, **139** (2016) 1-6.

[2] David R. Lide, *Handbook of Chemistry and Physics* **(**86th edition), CRC Press Inc., Boca Raton, 2005-2006, 12-1-12 -212.

[3] Yong Ki Cho, Gang Sam Kim, Young Sik Song, Tae Hong Lim and Donggeun Jung, *Thin Solid Films,* **548** (2013) 162-167.

[4] P. Blösch, S. Nishiwaki, L. Kranz, C. M. Fella, F. Pianezzi, T. Jäger, C. Adelhelm, E. Franzke, S. Buecheler, and A. N. Tiwari, *Solar Energy Materials & Solar Cells,* **124** (2014)10-16.

[5] L. Assmann, J.C. Berne`de, A. Drici, C. Amory, E. Halgand, and M. Morsli, *Applied Surface Science,* **246** (2005) 159-166.

[6] Filiz Keleş, Yavuz Atasoy, and Ayşe Seyhan**,** Mater. Res. Express **6** (2019) 126455.

[7] D. W. Hoffman and John A. Thornton, *Journal of Vacuum Science & Technology* **17**, (1980) 380-383.

[8] P. M. P. Salomé, J. Malaquias, P. A. Fernandes and A. F. da Cunha, *Journal of Physics D: Applied Physics*, **43 (34)** (2010), 345501-345507.

[9] John H. Scofield, A. Duda, and D. Albin, B. L. Ballard, and P. K. Predecki, *Thin Solid Films*, **260 (1)** (1995) 26-31.

[10] Junbo Gong, Yifan Kong, Jianmin Li, Xiangqi Wang, Yande Que, Zengming Zhang, Zejun Ding, and Xudong Xiao, *Energy Sci Eng.*,**7** (2019) 754-763.

[11] K. Aryal, H. Khatri, R. W. Collins, and S. Marsillac, *International Journal of Photoenergy*, **2012** (2012) 1-7.

[12] Jaymin Ray and T. K. Chaudhuri, *Journal of Optoelectronics and Advanced Materials*, **17 (5-6)** (2015) 634-639.

[13] C. Suryanarayana and M. Grant Norton, *X-Ray Diffraction A Practical Approach*, first ed., Springer Science + Business Media New York, (1998).

[14] Ju-Heon Yoon, SunghunCho, WonMokKim, Jong-Keuk Park, Young-Joon Baik, Taek Sung Lee, Tae-Yeon Seong, and Jeung-hyun Jeong, *Solar Energy Materials & Solar Cells*, **95** (2011) 2959-2964.

[15] J. R. Ray, N. M. Shah, M. S. Desai and C. J. Panchal**,** *Journal of Nano- and Electronic Physics*, **3** (1), 766-775 (2011).

[16] Kyung Hoon Yoon, Seok Ki Kim, R. B. V. Chalapathy, Jae Ho Yun, Jeong Chul Lee and Jinsoo Song, *Journal of the Korean Physical Society*, **45 (4)** (2004) 1114-1118.

[17] A. M. Hofer, J. Schlacher, J. Keckes, J. Winkler and C. Mitterer, *Vacuum*, **99** (2014) 149-152.

[18] Weimin Li, Xia Yan, Armin G. Aberle, and Selvaraj Venkataraj, *International Journal of Photoenergy,* **2016 (2016)** 1-10**.**

[19] Heejin Ahn, Dongchan Lee, and Youngho Um, *Appl. Sci. Converg. Technol,.* **26 (1)** (2017) 11-15.

[20] Majid Khan, Mohammad Islam, Aftab Akram, Zeming Qi, and Liangbin Li, *Materials Science in Semiconductor Processing*, **27** (2014) 343-351.

[21] S. R. Rondiya, A. V. Rokade, A. A. Jadhavar, S. M. Pandharkar, R. R. Kulkarni, S. D. Karpe, K. D. Diwate, and S. R. Jadkar, 2nd International

Conference on Emerging Technologies: Micro to Nano 2015 AIP Conf. Proc. 1724, 020089-1-020089-5.

[22] Eigo Takahashi, Shirish A. Pethe, and Neelkanth G. Dhere, *35th IEEE Photovoltaic Specialists Conference*, 20-25 JUNE 2010, Honolulu, HI, USA, (2010) 002478-002482.

[23] Xinyi Dai, Aijun Zhou, Lidong Feng, Ying Wang, Jin Xu and Jingze Li, *Thin Solid Films,* **567** (2014) 64-71.

[24] Y. C. Lin, W. T. Yen and L. Q. Wang, *Chinese Journal of Physics,* **50 (1)** (2012) 82-88.

[25] Amol C. Badgujar, Sanjay R. Dhage and Shrikant V. Joshi**,** *Thin Solid Films,* **589** (2015) 79-84.

[26] Subhash M. Pandharkar, Sachin R. Rondiya, Avinash V. Rokade and Bharat B. Gabhale, *Thin Film Solar Cells. Front. Mater*, **5:13** (2018) 1-6.

[27] M. Rekow, R. Murison, C. Dunsky, C. Dinkel, J. Pern, L. Mansfield, T. Panarello, and S. Nikumb, *25th European PVSEC/WCPEC-5 Exhibition, 6-10 September (2010),* Valencia, Spain, NREL/CP-5200-49411, (2010) 1-10,

[28] Richard Viskup**,** *High Energy and Short Pulses Laser,* IntechOpen Access book, **Chapter 12** (2016) 305-325**.**

[29] Shizhou Xiao, Benjamin Schöps, and Andreas Ostendorf, *Physics Procedia* **39** (2012) 594-602.

[30] Matthias Domke, Luigi Nobile, Stephan Rapp, Sasia Eiselen, Jürgen Sotrop, Heinz P. Huberb, and Michael Schmidt**,** *8th International Conference on Photonic Technologies LANE, Physics Procedia,* **56** (2014) 1007-1014.

[31] L. Berthe, M. Arrigoni, M. Boustie, J. P. Cuq-Lelandais, C. Broussillou, G. Fabre, M. Jeandin, V. Guipont and M. Nivard, *Nondestructive Testing and Evaluation,* **26 (3-4)** (2011) 303–317.

[32] Matthias Domke, Dominik FELSL, Stephan Rapp, Jürgen Sotrop, Heinz P. Huber, and Michael Schmidt, *Journal of Laser Micro/Nanoengineering* **10 (2)** (2015) 119-123.

[33] V. E. Fortov, V. V. Kostin, and S. Eliezer, *Journal of Applied Physics,* **70** (1991) 4524-4531.

[34] Pei Ming Yang, Yu Lung Lo, And Yuan Hao Chang, Applied Optics **55 (19)** (2016) 5001-5007.

[35] J. Bovatsek, A. Tamhankar, R. S. Patel, N. M. Bulgakova, J. Bonse, *Thin Solid Films*, **518** (2010) 2897-2904.

[36] Eric Schneller, Neelkanth G. Dhere, Juliana Shimada and Aravinda Kar, *Proc. of SPIE*, **8826** (2013) 88260C-1-88260C-6.

[37] Paulius Gečys, Gediminas Račiukaitis, Eimantas Miltenis, Alexander Braun, and Steffen, *Physics Procedia*, **12** (2011) 141-148.

[38] Reiner Witte, Bruno Frei, Stefan Schneeberger, Stephan Bücheler, Shiro Nishiwaki, Andreas Burnc, Martin Muralt, Valerio Romano, and Lukas Krainer**,** *Proc. of SPIE* **8607** (2016) 86071B-1-86071B-18.

[39] Ashwini Tamhankar, James Bovatsek, Gonzalo Guadano, and Rajesh Patel, *ICALEO***, 2009**, (2009) 1251-1259.

[40] Gerhard Heise, Andreas Börner, Marcel Dickmann, Marina Englmaier, Andreas Heiss, Matthias Kemnitzer, Jan Konrad, Regina Moser, Jörg Palm, Helmut Vogt, and Heinz P. Huber, *Prog. Photovolt: Res. Appl.*, **23** (2013) 1291-1304.

[41] David J. Hwang, Seungkuk Kuk, Zhen Wang, Shi Fu, Tao Zhang, Gayeon Kim, Won Mok Kim and Jeung hyun Jeong, *Appl. Phys. A*, **123 (55)** (2017) 1-11.

[42] K. L. Mittal, *Electrocomponent Science and Technology***, 3** (1976) 21-42.

[43] Abd El Hady B. Kashyout, Hesham M. A. Soliman, Hanaa Abou Gabal, Poussy Aly Ibrahim and Marwa Fathy, *Alexandria Engineering Journal*, **50** (2011) 57-63.

[44] Chee Yee Kwok, Tom Puzzer, Kwang Ming Lin and Jafar Haji-Babaei, **3241** (2014) 143-150.

[45] ASTM-D3359-09 Standard Test Methods for Measuring Adhesion by Tape Test.

[46] Brijesh Singh Yadav, Amol C. Badgujar, Sanjay R. Dhage, Solar Energy **157** (2017) 507-513.